IEEE Access
Multidisciplinary | Rapid Review | Open Access Journal

Received November 4, 2019, accepted November 18, 2019, date of publication November 22, 2019,
date of current version December 23, 2019.

Digital Object Identifier 10.1109/ACCESS.2019.2955296

3D SAR Image Background Separation Based on Seeded Region Growing

LIANG LI, XIAOLING ZHANG, (Member, IEEE), LING PU, LIMING PU, BOKUN TIAN, LIMING ZHOU, AND SHUNJUN WEI

School of Information and Communication Engineering, University of Electronic Science and Technology of China, Chengdu 611731, China

Corresponding author: Xiaoling Zhang (xlzhang@uestc.edu.cn)

This work was supported in part by the National Key Research and Development Program of China under Grant 2017YFB0502700, and in part by the National Natural Science Foundation of China under Grant 61671113, Grant 61501098, and Grant 61571099.

ABSTRACT The environmental interference and the noise in 3D synthetic aperture radar (SAR) image, considered as the background, are inescapable and ought to be eliminated. For 3D SAR image, there is a spatial separation of the target and the background. Therefore, it is possible to achieve the separation of the target and the background by image segmentation. Due to the complexity of the target shape and the large dynamic range of the SAR image, the background cannot be accurately separated through the amplitude information alone. In this paper, a method based on region growing is proposed to achieve 3D SAR image background separation utilizing the plural and the spatial information. The image enhancement matrix, constructed by the plural information of the SAR image, is implemented to improve the contrast of the image. The seeds are extracted by the weighted Otsu, and the weight is determined by the structure and amplitude information from the target. For the region growing, the growing process is achieved by the accumulation of the growing rate, which can suppress the growing of the noise. During the region growing, the stopping growing condition of each seed is independent and controlled by the seed threshold. The global threshold constrains the almost unrestricted growing of the seed whose amplitude is close to the noise amplitude. The results of the simulation and the experiments verify the performance of the proposed method is higher than that of the compared methods with three image evaluation criteria. Besides, we discuss the cost of computation and the influences of three important parameters to achieve a complete analysis.

INDEX TERMS Synthetic aperture radar (SAR), image segmentation, region growing, image denoising.

I. INTRODUCTION

Synthetic aperture radar(SAR) is an all-day and all-weather microwave detection technology, which has a wide range of application, such as remote sensing [1], [2], security check [3]–[9], and radar cross section (RCS) measurement [10]. Compared with the 2D SAR image, 3D SAR image contains three-dimensional spatial information, which provides the possibility to separate the object of interests and the others.

SAR imaging is not only influenced by environmental interference but also influenced by kinds of noise, such as speckle noise and system noise. Thus, it is necessary to eliminate the interference and noise to improve the quality of the SAR image. 2D SAR imaging is considered as an irreversible projection process that 3D space object is projected onto a 2D plane. Meanwhile, the noise and the interference are projected onto the same plane, which causes the target to be disturbed by the noise and affected by the interference. Therefore, using 2D SAR image denoising method [11]–[15] to alleviate the impact of noise and interference will result in loss of target information.

3D SAR imaging, the other kind of projection process, transforms the raw data from 3D echo space to 3D image space. In this projection process, the spatial information contained in the raw data is preserved, which means the target and the others can be separated spatially. Hence, it is possible to separate the interference and the noise from 3D SAR image with little loss of the target information. The interference and the noise are defined as the background in this paper. Thereby, the elimination of the interference and the noise is regarded as the separation of the

The associate editor coordinating the review of this manuscript and approving it for publication was Sudhakar Radhakrishnan.

background and can be solved by the image segmentation method.

Researchers have studied the image segmentation for a long time and brought several methods to live. Nobuyuki Otsu presents a classical segmentation method called Otsu based on the threshold selection in [16], which separates the background from the image according to the gray image feature. The Otsu segmentation method only exploits the image amplitude information, ignoring the other geometry and phase information provided by the 3D SAR image. When the noise and the target have the similar amplitude, this noise will be incorrectly classified as the target of interest.

To further use the image amplitude and geometry information, Rolf Adams provides another segmentation method, seeded region growing (SRG) in 1994 which has good robustness and low computational complexity [17]. SRG has been widely used in various fields, such as computer vision, medical science, and radar image processing. Many researchers also improve SRG to enhance the performance and the adaptability of the application in each field [18]–[27]. Shortly after SRG being proposed, 3D seeded region growing has been proposed and applied in the medical field [28]. Dehmeshki [29] uses seeded region growing to achieve the segmentation of pulmonary nodules in thoracic computed tomography (CT) scans. Fu [30] applies the 3D seeded region growing method to the segmentation of the spinal canal region in CT images. However, traditional seeded region growing is not applicable to the 3D SAR image background separation because of the high dynamic range of SAR image.

Deep learning has been concerned widely, and many image segmentation methods based on deep learning have been proposed [31]–[33]. Recently, some researchers combine SRG with deep learning to achieve image segmentation [34]–[37]. Data set is crucial for deep learning, and multiple public data sets appear in the field of computer vision and medical image processing. However, it is still difficult to obtain the data set of 3D SAR image. Thus, the background separation of 3D SAR image achieving by deep learning is hard to be performed currently.

Apart from environmental interference and kinds of noise, SAR imaging is also influenced by platform motion errors which result in the defocusing and the raising of side lobe amplitude [38], [39]. Affected by platform motion errors, the background separation is more difficult to be achieved.

In this paper, global seeded region growing (GSRG) is proposed to achieve the background separation of 3D SAR image, which takes advantage of the geometry information and the plural information. Scattering center model is the theoretical basis of SAR imaging [40]. Because the target of 3D SAR image consists of multiple discrete regions, the image continuity of 3D SAR image is worse than that of optical and medical images. Each discrete region of the target exists the initial seeds. Therefore, multiple seeded region growing is implemented to extract the whole target consisting of multiple discrete regions. High dynamic range is the characteristic of SAR image. For classic seeded region growing, the strong and weak target regions cannot be extracted at the same time, because the stopping growing threshold is determined by the region mean. For the proposed method, the stopping growing threshold of each seed is determined by the amplitude of this seed instead of the region mean. Thus, both strong and weak target regions are able to be extracted, which decreases the loss of the target details.

The proposed method consists of several main steps. To suppress the amplitude of the noise and the weak interference, image enhancement function, exploiting the real and the imagery information of the 3D SAR image, is implemented to increase the image contrast. The extraction of the seed information directly determines the performance of background separation. An Otsu-based method has been used to extract the seed information for the segmentation of medical image [37]. However, this method cannot stably extract usable seed information from 3D SAR image due to the complexity of the target shape and the high dynamic range of SAR image. Therefore, the weighted Otsu is applied to obtain the right seed information. The weight ensures the background information is almost not included in the initial seed information. The seed only contains the main information of the target, which is the basis for recovering the target details and separating the background. The growing rate function, being proportional to the amplitude of the seed and the amplitude of the current growing position, is implemented to suppress the growing rate of the noise. The growing state matrix, whose initial state is the initial seed matrix, stores the results of the growing rate for each generation. The seed will stop growing if there is no candidate position available to grow, or if the minimal difference between the candidate growing position amplitude and the seed amplitude is larger than the stopping growing threshold. During the region growing, the mask standard deviation is performed to reflect the image quality. While the backward difference of the mask standard deviation is lower than the global threshold, the region growing will be stopped to constrain the almost unrestricted growing of the seed whose amplitude is close to the noise amplitude.

In the field of SAR, there are few kinds of research on 3D SAR image segmentation at present. In the field of computer vision and medicine, 3D image segmentation has been researched for a long time. Unfortunately, these methods cannot achieve 3D SAR image background separation stably and accurately. Because the quality of 3D SAR image, influenced by the motion error and the environment interference, is usually lower than that of the optical and medicine image. Hence, we improve seeded region growing based on the characteristics of 3D SAR image. Regardless of robustness or accuracy, the performance of the proposed method is stronger than that of the comparison methods. The above will be demonstrated and verified in the simulation and experiment section.

The key contribution of the work can be summarized as follows. The image enhancement function is proposed to suppress the amplitude of the noise and the weak interference.

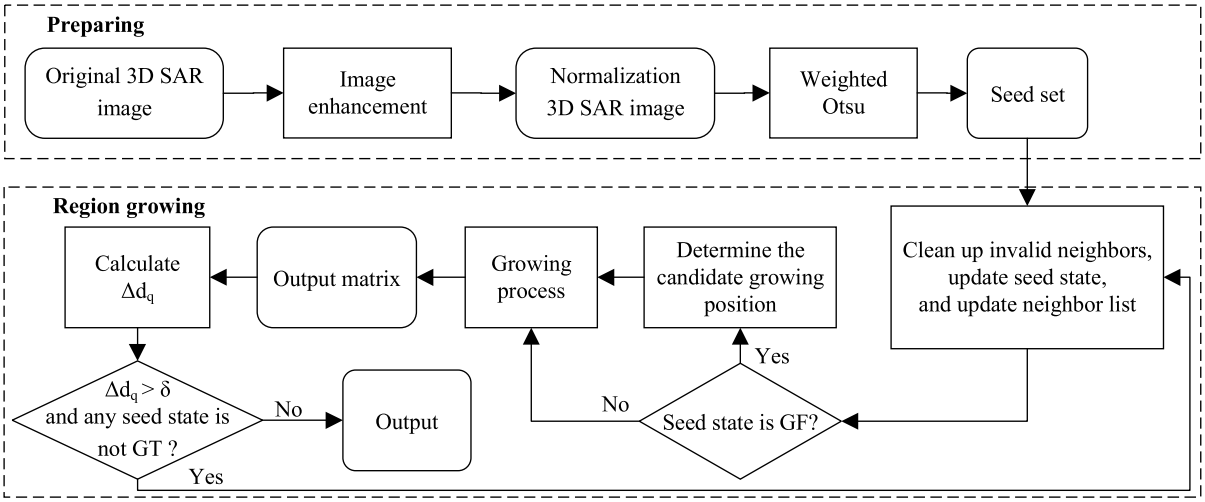

FIGURE 1. The overview of the proposed method. Δd_q denotes the backward difference of the mask standard deviation. δ denotes the global threshold.

The weight Otsu is applied to overcome the complexity of the target shape and the large dynamic range of SAR image in seed selection. The growing rate function is proposed to suppress the increasing rate of the noise. The independent seed threshold and the global threshold are applied to control the growing process, and ensure the whole target is extracted with the noise suppressed.

The rest of this paper is organized as follows. In section 2, we describe the algorithm and the main theory of the proposed method. In section 3, the results of the simulation and the experiments verify the effectiveness and the performance of the proposed method with four comparison methods by three image evaluation criteria. Simultaneously, we discuss the computational cost and the influences of three important parameters on the stability of the algorithm. In section 4, the main conclusions and the limitation are summarized.

II. METHOD

A. ALGORITHM

The algorithm and various main steps of the proposed method are described in this part. The overview is illustrated in Fig.1. The algorithm includes two stages: the preparing and the region growing. The preparing stage consists of three steps: the image enhancement, the normalization of the enhanced image, and the generation of the seed set by weighted Otsu. The purpose of the preparing stage is to extract the initial seeds. The region growing stage consists of four steps: the cleaning and the updating of the neighbor list, the determination of the candidate growing position, the growing process, and the calculation of the backward difference of the mask standard deviation.

For the preparing, the input includes the original SAR image S. Two parameters, the enhancement coefficient γ and the weight α, are set manually. Firstly, after calculating the Hadamard product of the image enhancement matrix P and the matrix S, the result is the enhanced image S_A (refer to (1) and (3)). Then, the amplitude of the matrix S_A is extracted and normalized, which obtains the matrix I. The weighted Otsu is implemented on I to generate the seed set $\tilde{E}$ which stores the amplitude and position information (refer to (4) and (5)). So far, the preparing work has been finished.

For the region growing, the detailed description is illustrated in Algorithm 1. The input of the region growing stage includes the original SAR image S, the normalization image I, and the seed set $\tilde{E}$. The growing coefficient K, the seed threshold μ, and the global threshold δ are set manually. The neighbor list $\Gamma_n(l)$ instead of the sequentially sorted list (SSL) is applied to store the information of the lth candidate position of the nth seed. The neighbor list is a set composed of the cells where the position and the amplitude information of the candidate positions are stored in. The growing state matrix G records the growing rate of each seed for each generation, and the growing state g_{xyz} is the element in the growing state matrix G. Before the region growing, the neighbor list $\Gamma_n(l)$ and the growing state matrix G need to be initialized. The initial neighbor list $\Gamma_n(l)$ is an empty set, and the initial growing state matrix G is equal to the initial seed matrix E. Three seed states, the growing unfinished (GU), the growing finished (GF), and the growing terminated(GT), are defined to indicate the growing state of the seed. The GU means the seed is still growing in the current position. The GF means the seed is finding the next position. The GT means the seed does not satisfy the growing condition and will not participate in the growing.

For each generation, cleaning up the neighbor list and updating the seed state is the first and necessary step. If the growing of several candidate positions is finished by other seeds, these candidate positions need to be removed from the neighbor list. The seed state is updated according to the growing state of the position where the seed is located in. Then, the neighbors will be selected and added to the neighbor list.

Algorithm 1 Region Growing

Require: The original SAR image S; the normalized amplitude matrix I; the seed set $\tilde{E}$; the growing coefficient K; the seed threshold μ; the global threshold δ;

Ensure: The matrix $\tilde{I}$;

Initialize $\Gamma_n(l)$ and G;
while $\nabla d_q > \delta$ **do**
  for n from 1 to N **do**
    if $\Xi(n) =$ GT **then**
      end the loop;
    end if
    If $g_{x'y'z'} \geq 1$, remove the neighbor whose position is (x', y', z') stored in $\Gamma_n(l)$;
    if no neighbors can be put to the neighbor list and $\Gamma_n(l) = \varnothing$ **then**
      $\Xi(n) =$ GT, and end the loop;
    end if
    if $\Xi(n) =$ GF **then**
      Put the neighbor whose growing state is lower than 1 into the neighbor list $\Gamma_n(l)$;
      $\hat{T}_n(l) = \hat{\Gamma}_n(l) - E_n$ (see (6));
      $l' = \arg\min_l \{\hat{T}_n(l)\}$, and extract the position $(x_{new}, y_{new}, z_{new})$ in $\Gamma_n(l')$;
      if $\hat{T}_n(l') > T_n$ **then**
        $\Xi(n) =$ GT, and end the loop;
      end if
      Calculate the G_r and add it to g_{xyz} (see (8) and (9));
      Update the seed status Ξ based on g_{xyz} and the seed position: $(x, y, z) \leftarrow (x_{new}, y_{new}, z_{new})$;
    else if $\Xi(n) =$ GU **then**
      Calculate the G_r, and add it to g_{xyz} (see (8) and (9));
      Update seed status Ξ based on g_{xyz};
    end if
  end for
  Calculate $\tilde{I}$ and ∇d_q (see (14) and (20));
end while
return $\tilde{I}$;

The set $\hat{T}_n(l)$ is the difference between the amplitude of the neighbor list and the amplitude of the nth seed (refer to (6)). l' is calculated by (7), and $\hat{T}_n(l')$ is the minimum value in $\hat{T}_n(l)$. The position stored in $\Gamma_n(l')$ is selected as the candidate growing position. Then, the growing rate $G_r(x, y, z, E_n)$ is calculated and added to the growing state g_{xyz} (refer to (8) and (9)). For the growing state matrix, there are two growing states: $0 < g_{xyz} < 1$ indicates that the position (x, y, z) is under growing and $g_{xyz} \geq 1$ indicates that the growing of the position (x, y, z) has been finished. After that, the seed state will convert to GU if the growing state is $0 < g_{xyz} < 1$, and the seed state will convert to GF if the growing state is $g_{xyz} \geq 1$. The output matrix $\tilde{I}$ is the Hadamard product of the original SAR image S and the matrix G after round down $\lfloor \cdot \rfloor$ (refer to (14)). Then, the backward difference of the mask standard deviation ∇d_q of the output matrix is calculated to reflect the image quality (refer to (20)). These steps are iterated for several generations until $\nabla d_q < \delta$ or all seed states convert into the GT. The output matrix $\tilde{I}$ of the last generation is the processed image. So far, background separation has been finished.

B. IMAGE ENHANCEMENT FUNCTION

To improve the effectiveness of the background separation, an image preprocessing is needed to suppress the amplitude of the noise and weak interference. Therefore, the image enhancement function, constructed by the real part and imaginary part of 3D SAR image, is applied to achieve the preprocessing.

U is defined as a plural matrix. The matrix U_r and the matrix U_i are the real part and the imaginary part of the matrix U respectively. The image enhancement function is expressed as

$$f(U_r, U_i) = exp\left(\frac{\gamma \cdot (|U_r + U_i| + |U_r - U_i|)}{\max(|U_r + U_i| + |U_r - U_i|)}\right) \quad (1)$$

where γ named as the enhancement coefficient denotes the coefficient to control the enhancement effect, $max(\cdot)$ denotes the maximum of all matrix elements.

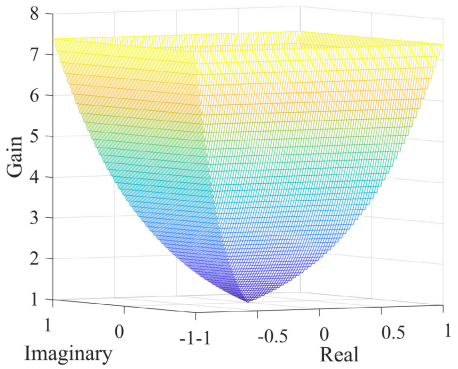

FIGURE 2. Image enhancement function ($\gamma = 2$).

The result of the image enhancement function is a gain matrix. The relation between the gain and amplitude of an element is shown in Fig.2. Assuming u_r and u_i are the real part and the imaginary part of the element $U(x_p, y_p, z_p)$ respectively, the gain of the element $U(x_p, y_p, z_p)$ is exponentially related to the maximum of u_r and u_i. Therefore, the gain of the noise and weak interference with low amplitude is lower than the gain of the target with high amplitude.

The amplitude normalization has been achieved in the image enhancement function. Although the amplitude range of different SAR images has a huge difference, the gain of one element is not influenced by the absolute amplitude and proportional to the relative amplitude of this element in the matrix. Moreover, when γ is fixed, the gain of the maximum value is also constant. Hence, the image enhancement function has good robustness.

After SAR imaging, the original SAR image is expressed as the matrix $S(x, y, z), x \in X, y \in Y, z \in Z$. The matrix V_r and the matrix V_i are the real part and the imaginary part of the original SAR image S respectively. The image enhancement matrix P is calculated by the image enhancement function, which is expressed as

$$P = f(V_r, V_i). \tag{2}$$

The enhanced SAR image S_A is the result of the Hadamard product of the matrix S and the image enhancement matrix P, which is expressed as

$$S_A = S \circ P \tag{3}$$

where $\circ$ denotes the Hadamard product.

C. SEED SELECTION

The initial seeds determine which areas are reserved, therefore, it is necessary to ensure that little background is included in the initial seeds. The selection of the initial seeds can be achieved by manual selection and automated methods. Although the result of manual selection is excellent, it is hard to be applied because manual selection has a huge time consumption. The result of the automated method can meet the requirements of target extraction [37], meanwhile, the time consumption of the automated method is much lower than that of the manual selection.

Generally, the amplitude of the target is higher than that of the background. Therefore, the selection of the initial seeds can be achieved by the image amplitude information. For 3D SAR image, due to the complexity of the target shape and the large dynamic range of SAR image, the selection of the right seeds cannot be achieved by Otsu stably. Therefore, a semi-automatic method combined with the advantage of the manual and automated method is applied to achieve the selection of the initial seeds, which has high accuracy and low time consumption.

The amplitude of the enhanced image S_A is extracted and normalized, and the result is the matrix $I \in R^{X \times Y \times Z}$ consisting of the element $i_{xyz} \in [0, 1]$. The seed generating threshold θ_I is used to extract the initial seeds form the matrix I, which is expressed as

$$\theta_I = \alpha \cdot T_{otsu} \tag{4}$$

where $\alpha(\alpha \geq 1)$ named as the weight denotes the coefficient to ensure the background is excluded from the initial seeds as much as possible, T_{otsu} denotes the threshold calculated by Otsu [16]. The setting of the weight α is based on the effect of the background elimination of the initial seeds. If the background has been completely eliminated by the threshold T_{otsu}, the weight α will not work. At this time, the weight α is equal to 1, and the seed generating threshold θ_I is equal to T_{otsu}. If the background cannot be completely eliminated by the threshold T_{otsu}, the weight α is used to increase the seed generating threshold θ_I to ensure the initial seeds contain little background. The number of the initial seeds is inversely proportional to the seed generating threshold.

The initial seed matrix $E \in R^{X \times Y \times Z}$ consists of the initial seed e_{xyz} which is calculated by the seed generating threshold θ_I,

$$e_{xyz} = \begin{cases} i_{xyz} & i_{xyz} \geq \theta_I \\ 0 & i_{xyz} < \theta_I. \end{cases} \tag{5}$$

The matrix E contains main target information, and the details of the target will be supplemented by the region growing. The seed amplitude E_n is extracted from the initial seed matrix E and restored in seed set $\tilde{E} = \{E_n | E_n \in E, n = 1, 2, \ldots, N\}$. N denotes the number of the initial seeds.

D. NEIGHBORS AND GROWING PROCESS

Before the growing process, the neighbors are selected by the template and stored in the neighbor list. The template, N6, is used to obtain the neighbors, which is shown in Fig.3. The current position of the seed is marked by the red block, and the neighbors are marked by the yellow blocks. Assuming that the current position is (x_s, y_s, z_s), the neighbors of the position (x_s, y_s, z_s) are $(x_s \pm 1, y_s, z_s)$, $(x_s, y_s \pm 1, z_s)$, $(x_s, y_s, z_s \pm 1)$. For nth seed, the position and the amplitude information of the neighbors are stored in the neighbor list $\Gamma_n(l), l = 1, 2, \ldots, L$. L denotes the number of the neighbors stored in the neighbor list.

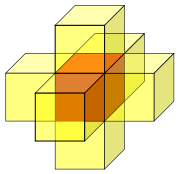

FIGURE 3. The template N6 for obtaining neighbors.

For SRG [17], the selection of the next growing position and the condition of the stopping growing are determined by the minimal difference between the amplitude of the candidate positions and the region mean. If the region mean is influenced by the noise, the region mean will be close to the noise mean finally, which causes the number of the noise increases continuously. To solve this problem, the region mean is replaced by the initial seed amplitude. Thereby, the selection of the next growing position and the condition of the stopping growing are not affected by the noise, and independent for each seed. Hence, the growing process of the seed will not be influenced by noise. For nth seed, the difference between the amplitude of the neighbor list and the amplitude of the nth seed is expressed as

$$\hat{T}_n(l) = \hat{\Gamma}_n(l) - E_n \tag{6}$$

where $\hat{\Gamma}_n(l)$ denotes the amplitude in $\Gamma_n(l)$. Then, $\hat{T}_n(l')$, the minimum value of $\hat{T}_n(l)$, needs to be found out. The corresponding position l' is extracted,

$$l' = \arg\min_l \{\hat{T}_n(l)\}. \tag{7}$$

The position stored in $\Gamma_n(l')$ is selected as the next growing position.

For SRG [17], the growing of each seed is completed in each generation. Namely, the pixels with different amplitude have the same growing rate. In this paper, the amplitude information is utilized to differentiate the growing rate of the pixels. Namely, the pixels with different amplitudes have different growing rates. The growing of each seed becomes an amplitude accumulation process described by the growing rate function and the growing state matrix.

The growing rate is determined by the amplitude of the seed and the image amplitude of the current growing position. The growing rate $G_r(x, y, z, E_n)$ of the nth seed in position(x, y, z) is calculated by the growing rate function, which is expressed as

$$G_r(x, y, z, E_n) = \frac{\exp\left((\eta + E_n)/K\right)}{\left(\exp\left(\left(max(I) + max(\tilde{E})\right)/K\right)\right)} \tag{8}$$

where η denotes the amplitude of the matrix I in the position (x, y, z), E_n denotes the amplitude of the nth seed, K named as the growing coefficient denotes a coefficient to control the suppression effect to low amplitude pixel, and $max(\cdot)$ denotes the maximum of all elements in matrix or set. Fig.4 illustrates the relationship between the growing rate and the variable. The growing rate is exponentially related to E_n and η. With the decreasing of the coefficient K, the curvature of the growing rate function is increasing, which results in the increasing of the suppression effect for the low amplitude pixels. The growing rate is a normalized result, and the normalization enhances the robustness of the growing rate function. Generally, the amplitude of the noise is lower than that of the target. Therefore, the growing rate of the noise is lower than that of the target.

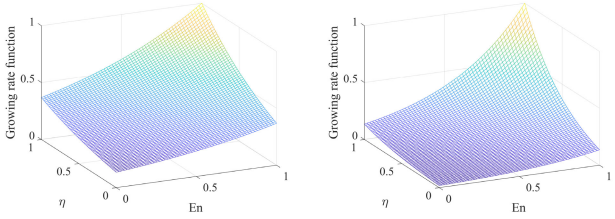

(a) K=1 (b) K=0.5

FIGURE 4. The relationship between the growing rate with η and E_n.

The growing state matrix $G \in R^{X\times Y\times Z}$ records the accumulation results of each seed for each generation, and g_{xyz} is the element in G. And the initial growing state matrix G is equal to the initial seed matrix E. For the effective seed in each generation, the growing rate $G_r(x, y, z, E_n)$ in the position (x, y, z) is calculated by (8) and added to g_{xyz}. This accumulation process is expressed as

$$g_{xyz} = g_{xyz} + G_r(x, y, z, E_n). \tag{9}$$

For the matrix G, $0 < g_{xyz} < 1$ means that the position (x, y, z) is under growing, and $g_{xyz} \geq 1$ means that the growing of the position (x, y, z) has been finished. The accumulation process of high amplitude pixel is faster than that of low amplitude pixel. Generally, the target amplitude is higher than the noise amplitude. After the same generations, the increasing number of the target pixels is more than that of the noise pixels. Namely, the growing process achieves the suppression of the noise.

When multiple seeds choose the same pixel as the next growing position, the growing rate of these seeds will be added to the same position in the growing state matrix. For example, there are n seeds to choose the position (x_0, y_0, z_0) as the growing position. The growing rate of each seed is $G_{r1}, G_{r2}, \ldots, G_{rn}$. The growing state of the position (x_0, y_0, z_0) is expressed as

$$g_{x_0,y_0,z_0} = g_{x_0,y_0,z_0} + G_{r1} + G_{r2} + \ldots + G_{rn}. \tag{10}$$

When $g_{x_0,y_0,z_0} \geq 1$, all n seeds will stop the growing process and select the next growing position. Thus, the growing processing of one seed will not be obstructed by the other seeds. And if one of these seeds finishes the growing process, the other seeds will be stopped. The selection of the next growing position for each seed is independent.

E. STOPPING GROWING CONDITION OF THE SEED

The seed threshold is defined as $\mu \in [0, 1]$, the stopping growing threshold of the nth seed is expressed as

$$T_n = \mu \cdot E_n. \tag{11}$$

After calculating the stopping growing threshold of the N seed by (11), the stopping growing threshold set $\tilde{T}$ is generated, and $\tilde{T} = \{T_n, n = 1, 2, \ldots, N\}$. For nth seed, the difference between the amplitude of the neighbor list and the amplitude of the seed is $\hat{T}_n(l)$. When the minimum element in $\hat{T}_n(l)$ is larger than the threshold T_n, the nth seed state will be converted into the growing terminated (GT) state from the GF state. The seed whose state is the GT is considered as the invalid seed, which means the seed does not satisfy the growing condition and will not participate in the growing process until the whole region growing is completed.

It is necessary to decrease the computation cost as much as possible because of the high computation of 3D image process. The application of the GT state makes invalid seeds not participate in the growing process, which is effective to improve computing efficiency.

In the other two cases, the seed state will also be converted into the GT. After the generating of the seed set $\tilde{E}$, the state of the seed that no neighbors can be put into the neighbor list is converted into the GT. At the beginning of each generation, the seed state will be converted into the GT if no neighbors can be put into the neighbor list and if the neighbor list is empty. Simultaneously, the effectiveness of all seeds will be examined, and only the effective seed whose state is not the GT state can participate in the growing process.

F. GLOBAL THRESHOLD

For SAR image, it is possible that the amplitude of the target details is close to the amplitude of the noise. When the region growing is only controlled by the stopping growing threshold, the segmentation result will contain lots of noise, which causes low image quality. Therefore, the global threshold which can control the image quality is applied to reduce the influence of noise.

The image evaluation function is usually applied to reflect the image quality quantitatively, such as the standard deviation(SD), the peak signal-to-noise ratio(PSNR), and the structural similarity (SSIM). While the region growing is processing, the image evaluation is applied to reflect the quality of the processed image timely. When the result of the image evaluation function is lower than the global threshold, the growing process of all seeds will be terminated immediately to control the quality of the segmentation result.

The standard deviation is considered as the image evaluation function because of low computational complexity. The standard deviation, being proportional to the image quality, reflects the amplitude dispersion of each pixel relative to the image mean. The standard deviation of the processed image for qth generation is expressed as

$$\tilde{D}_q = \sqrt{\frac{1}{N}\sum_{x=1}^{X}\sum_{y=1}^{Y}\sum_{z=1}^{Z}\left(\left|\tilde{i}_q(x,y,z)\right| - \bar{I}_q\right)^2} \tag{12}$$

$$\bar{I}_q = \frac{1}{N}\sum_{x=1}^{X}\sum_{y=1}^{Y}\sum_{z=1}^{Z}\left|\tilde{i}_q(x,y,z)\right| \tag{13}$$

where $N{=}X\times Y\times Z$, $|\cdot|$ denotes the complex magnitude of the element, $\tilde{i}_q(x,y,z)$ denotes the element in the qth generation output matrix $\tilde{I}_q$. And $\tilde{I}_q$ is calculated by

$$\tilde{I}_q = S \circ \lfloor G_q \rfloor \tag{14}$$

where $\lfloor\cdot\rfloor$ denotes the round down, G_q denotes the growing state matrix G in the qth generation. The round down indicates that the pixel whose value is equal to or larger than 1 is set as 1 and the pixel whose value is lower than 1 is set as 0.

The standard deviation is not suitable for 3D SAR image evaluation. Because 3D SAR image is a sparse matrix composed of multiple scattering centers, most pixels in the output matrix are zero, thereby, the standard deviation cannot reflect the image quality accurately. Therefore, the mask standard deviation (MSD) is applied to evaluate the quality of the processed image. Non-zero pixels are marked as the active pixels and used to calculate the MSD. The mask standard deviation of the processed image for the qth generation is expressed as

$$d_q = \sqrt{\frac{1}{N_I}\sum_{x=1}^{X}\sum_{y=1}^{Y}\sum_{z=1}^{Z}\left(\left|\tilde{i}_q(x,y,z)\right| - \hat{I}\right)^2} \tag{15}$$

$$\hat{I} = \frac{1}{N_I}\sum_{x=1}^{X}\sum_{y=1}^{Y}\sum_{z=1}^{Z}\left|\tilde{i}_q(x,y,z)\right| \tag{16}$$

where N_I is the number of non-zero pixels in the matrix $\tilde{I}_q$. The mask standard deviation of the initial seeds is expressed as

$$d_S = \sqrt{\frac{1}{N_S}\sum_{x=1}^{X}\sum_{y=1}^{Y}\sum_{z=1}^{Z}\left(\left|\tilde{i}_E(x,y,z)\right| - \hat{E}\right)^2} \tag{17}$$

$$\hat{E} = \frac{1}{N_S}\sum_{x=1}^{X}\sum_{y=1}^{Y}\sum_{z=1}^{Z}\left|\tilde{i}_E(x,y,z)\right| \tag{18}$$

where N_S denotes the number of non-zero pixels in the matrix $\tilde{I}_E$, $\tilde{i}_E(x,y,z)$ denotes the element in the matrix $\tilde{I}_E$.

$$\tilde{I}_E = S \circ \lceil E \rceil \tag{19}$$

where $\lceil\cdot\rceil$ denotes the round up. The MSD is not influenced by a large number of zero pixels in the output matrix, thus, the accuracy of MSD to reflect image quality is higher than that of the SD.

Because the amplitude range of different SAR images has a large difference, the MSD for different SAR images has a huge difference. That the MSD is related to the image amplitude causes the instability of the evaluation and a tough challenge to adjust the global threshold. Therefore, the backward difference of the MSD is applied as the evaluation criterion reflecting the changing of image quality clearly. Assuming that the qth and the $q-1$th generation of the MSD are d_q and d_{q-1}, the backward difference of the MSD is expressed as

$$\nabla d_q = \left|\frac{d_q - d_{q-1}}{d_q}\right|. \tag{20}$$

For the first generation, d_0 is the MSD of the initial seeds d_S. For different images, the backward difference of the MSD is robust, because the differential result of the MSD has been normalized. The global threshold δ is set based on the target details needed to be preserved in the image. With the increase of the generation, the proportion of the target detail pixels in the increased pixels is decreasing, and the proportion of the background pixels in the increased pixels is increasing. Thereby, ∇d_q is decreasing continuously due to the decreasing of the amplitude of the increased pixels. When the condition $\nabla d_q < \delta$ is satisfied, the region growing will be terminated. Thus, the target details are recovered, simultaneously, the increasing of the noise is suppressed.

The region growing will be stopped when all seed states are the GA or the backward difference of the MSD is smaller than the global threshold. The result of background separation is the output matrix in the last generation.

III. EVALUATION CRITERIA

Three image quality evaluation criteria, the relative foreground area error (RAE), the misclassification error (ME) [41], [42], and the intersection over union (IoU), are implemented to analyze the performance of the segmentation method quantitatively.

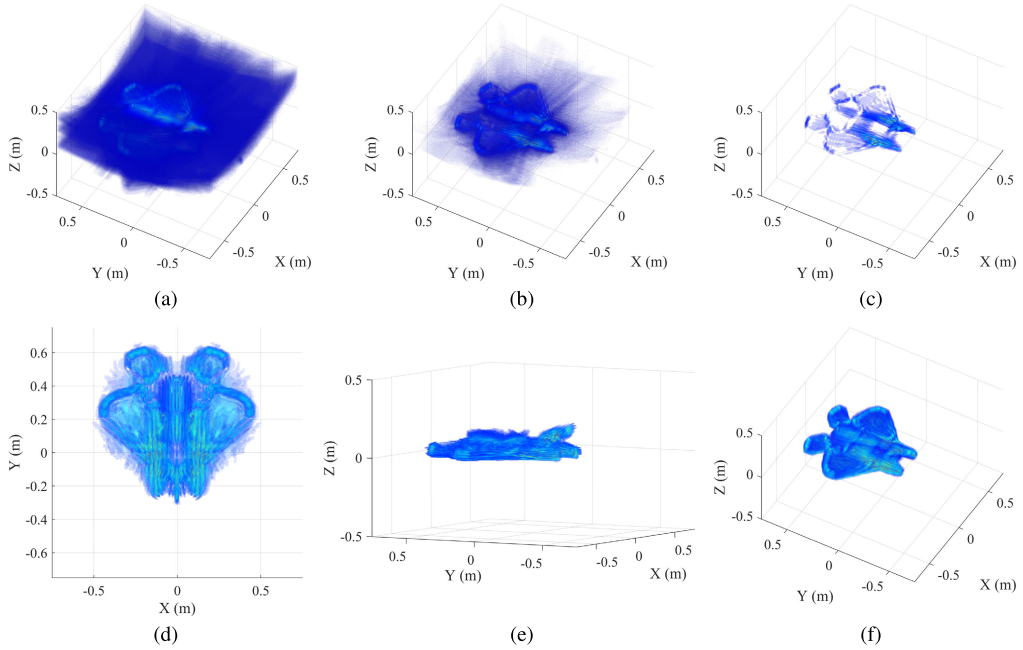

FIGURE 5. The process and the results of the proposed method. (a) The original SAR image. (b) The enhanced image. (c) The seed matrix. It is generated by the weighted Otsu. (d) The processed image by GSRG (angle 1). (e) The processed image by GSRG (angle 2). (f) The ground truth. It is considered the standard in the evaluation criteria.

The RAE is used to reflect the misclassification percentage of the foreground. In this paper, the foreground denotes the target area. According to [42], we redefine the expression of the RAE,

$$RAE = \frac{|A_T| - |A_0 \cap A_T|}{|A_T|} \tag{21}$$

where A_0 denotes the foreground of the ground truth, A_T denotes the foreground of the processed image, $\cap$ denotes the intersection operation, $|\cdot|$ denotes the number of pixels in area. The range of the RAE is [0, 1]. The RAE is inversely proportional to the performance of the segmentation method. And a good segmentation method has low RAE.

The RAE that only reflects the percentage of foreground misclassification cannot evaluate the algorithm comprehensively. Therefore, the ME is implemented to achieve a comprehensive evaluation, which refers to the total misclassification percentage of the foreground and the background. The ME is expressed as

$$ME = 1 - \frac{|B_0 \cap B_T| + |A_0 \cap A_T|}{|B_0| + |A_0|} \tag{22}$$

where B_0 denotes the background of the ground truth, B_T denotes the background of the processed image. The range of the ME is [0, 1]. The ME is inversely proportional to the performance of the segmentation method. The better the performance of the segmentation method is, the closer the ME is to zero.

The IoU is generally used to reflect the correlation between the segmentation result and the ground truth, which is expressed as

$$IoU = \frac{A_0 \cap A_T}{A_0 \cup A_T} \tag{23}$$

where $\cup$ denotes the union operation. The IoU is proportional to the performance of the segmentation method.

IV. SIMULATION

A. PROCESSING ON SIMULATION DATA

1) SETTINGS

For the generation of the simulation data, the echo of the aircraft model is calculated by FEKO, a professional electromagnetic simulation software. The length of the model is 2.76 meters. The carrier frequency is 10 GHz, and the bandwidth is 3 GHz. The raw echo is generated by a 3 m $\times$ 3 m planar array with 101 $\times$ 101 elements. The back projection (BP) is used to achieve the SAR imaging, and the size of the original SAR image is 250$\times$250$\times$151. The parameters of the proposed method are set as follows: The weight α is 1.6. The seed threshold μ is 0.7. The global threshold δ is 0.0001. The growing coefficient K is 1. The enhancement coefficient γ is 2. Four comparison methods are implemented: Otsu [16], Kittler and Illingworth [43], GMM-HMRF [44], and MICO [45].

2) RESULT

The processing and the results of GSRG are shown in Fig.5. Fig.5(a) is the original SAR image which contains lots of side lobes, and the target is covered by these side lobes. The enhanced image is depicted in Fig.5(b), and the contrast

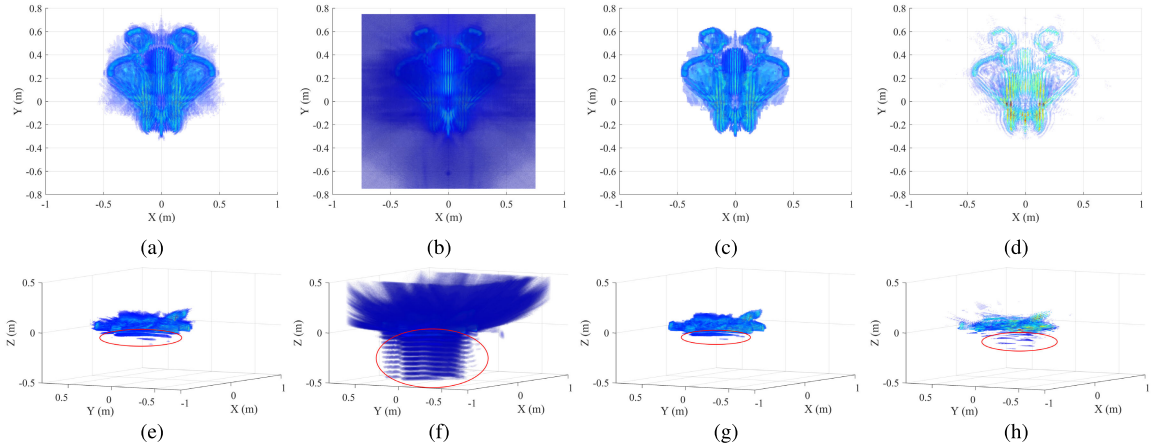

FIGURE 6. The simulation results of the comparison methods. (a)Otsu (angle 1). (b)Kittler (angle 1). (c)GMM-HMRF (angle 1). (d)MICO (angle 1). (e)Otsu (angle 2). (f)Kittler (angle 2). (g)GMM-HMRF (angle 2). (h)MICO (angle 2). The grating lobe is marked by the red solid circle.

of the enhanced image is stronger than that of the original image. The seed matrix generated by the weighted Otsu is displayed in Fig.5(c). The results of GSRG are shown in Fig.5(d) and (e). Most backgrounds are separated by GSRG, and there are only a few side lobes around the wing.

The results of Otsu, Kittler, GMM-HMRF, and MICO are displayed in Fig.6. For Fig.6(b) and (f), Kittler has no effect on background separation. Conversely, the result of MICO loses lots of the target information, which is shown in Fig.6(d). Compared with the result of GSRG, the result of Otsu and GMM-HMRF contains more side lobes, which is shown in Fig.5(d), Fig.6(a), and Fig.6(c). For Fig.5(e), the result of GSRG does not contain strong side lobes under the wings. Differently, the result of Otsu, Kittler, GMM-HMRF, and MICO still contains strong side lobes marked by the red solid circle, which is shown in Fig.6(e), (f), (g), and (h). Therefore, the performance of the proposed method is higher than that of the comparison methods.

The performance analysis of these five methods is implemented by three image evaluation criteria, the RAE, the ME, and the IoU. The ground truth, as the reference image for the evaluation, is derived from the original SAR image based on the optical image, which is shown in Fig.5(f). For Fig.7, 200 independent experiments are performed on GMM-HMRF and MICO respectively. Obviously, the stability of GMM-HMRF and MICO is poor. Table 1 reports the performance analysis results of five methods. Due to the poor stability of GMM-HMRF and MICO, the RAE, ME, and IoU of GMM-HMRF and MICO shown in Table 1 refer to the mean of 200 independent experiments. The RAE of GSRG is 15.67% lower than that of Otsu, 76.27% lower than that of Kittler, 18.92% lower than that of GMM-HMRF, and 12.19% lower than that of MICO. The ME of GSRG is 0.31% lower than that of Otsu, 71.07% lower than that of Kittler, 19.60% lower than that of GMM-HMRF, and 0.75% lower than that

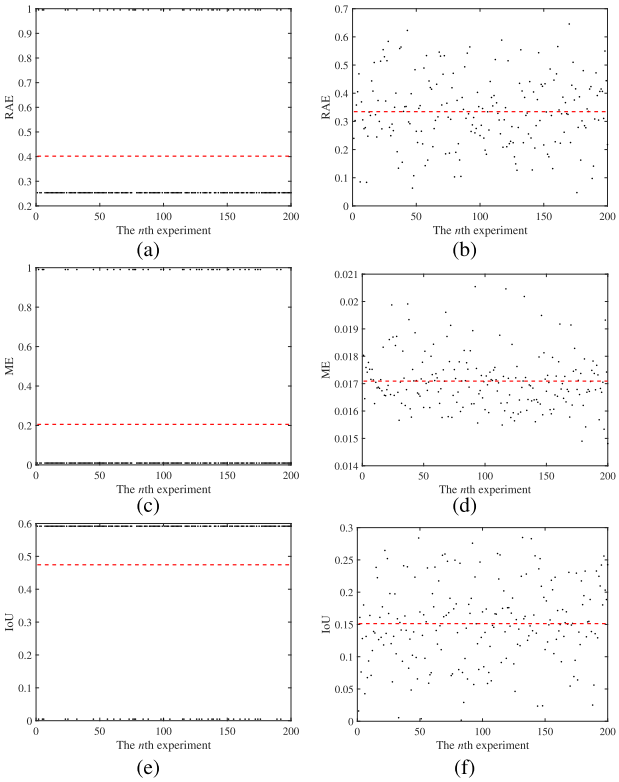

FIGURE 7. The results of 200 independent experiments of GMM-HMRF and MICO. (a)The RAE of GMM-HMRF. (b)The RAE of MICO. (c)The ME of GMM-HMRF. (d)The ME of MICO. (e)The IoU of GMM-HMRF. (f)The IoU of MICO.

of MICO. The IoU of GSRG is 4.39% higher than that of Otsu, 52.97% higher than that of Kittler, 8% higher than that of GMM-HMRF, and 40.31% higher than that of MICO. Hence, the performance of GSRG is always better than that of the comparison methods. In addition, the performance of Otsu is close to that of GSRG, and the performance of the other three comparison methods is unacceptable.

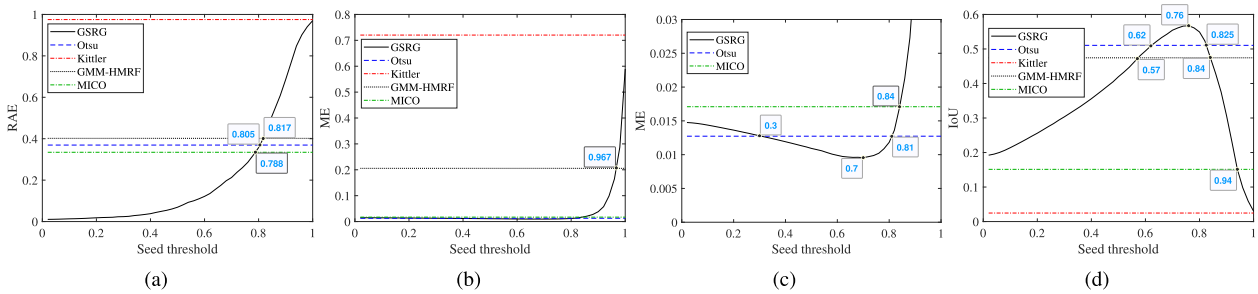

FIGURE 8. The analysis results of the seed threshold. (a)The RAE. The intersection of GSRG and MICO is at (0.788,0.335). The intersection of GSRG and Otsu is at (0.805,0.369). The intersection of GSRG and GMM-HMRF is at (0.817,0.402). (b)The ME. The intersection of GSRG and GMM-HMRF is at (0.967,0.206) (c)The partially enlarged image of the ME curve. The intersections of GSRG and Otsu are at (0.3,0.013) and (0.81,0.013). The intersection of GSRG and MICO is at (0.84,0.017). The minimal ME of GSRG is at (0.7,0.010). (d)The IoU. The intersections of GSRG and GMM-HMRF are at (0.57,0.474) and (0.84,0.474). The intersections of GSRG and Otsu are at (0.62,0.511) and (0.825,0.511). The intersection of GSRG and MICO is at (0.94,0.151). The maximal IoU of GSRG is at (0.76,0.567).

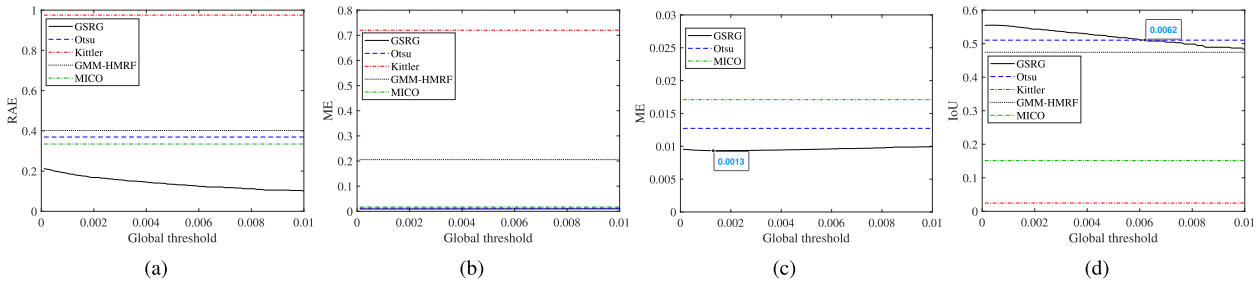

FIGURE 9. The analysis results of the global threshold. (a)The RAE. (b)The ME. (c)The partially enlarged image of the ME curve. The minimal ME of GSRG is at (0.0013,0.009). (d)The IoU. The intersection of GSRG and Otsu is at (0.0062,0.511).

TABLE 1. The analysis results of the simulation.

Method	RAE	ME	IoU
GSRG	21.26%	0.96%	55.44%
Otsu	36.93%	1.27%	51.05%
Kittler	97.53%	72.03%	2.47%
GMM-HMRF	40.18%	20.56%	47.44%
MICO	33.45%	1.71%	15.13%

TABLE 2. The setting of the single parameter analyses.

Analyzed parameter	μ	δ	α
Seed threshold μ	[0.02,1]	0.0001	1.6
Global threshold δ	0.7	[0.0001,0.01]	1.6
Weight α	0.7	0.0001	[1,2]

B. THE SINGLE PARAMETER ANALYSIS

There are 5 variable parameters in the proposed method. The enhancement coefficient γ controls the enhancement effect on the image contrast. The weight α is inversely proportional to the number of the initial seeds generated by the weighted Otsu. The growing coefficient K controls the suppression effect on low amplitude pixel of the growing rate function. The seed threshold μ controls the difference in amplitude between the current growing pixel and the initial seed when the growing of the seed is stopped. The global threshold δ controls the image quality when the region growing is stopped, which is proportional to the image quality of the segmentation result.

Three parameters, the seed threshold μ, the global threshold δ, and the weight α, are selected and analyzed, which have a direct influence on the results. The other two parameters, the growing coefficient K and the enhancement coefficient γ, are controlled with $K = 1$ and $\gamma = 2$.

In each analysis, two parameters are fixed, one parameter varies within the settings. The fixed parameters are the same as the parameters set in the part A. The setting of the parameter analysis is specified in Table 2. The analyses are illustrated in Fig.8, Fig.9, and Fig.10. GSRG is marked by the black solid line. Otsu is marked by the blue dashed line. Kittler is marked by the red chain line. GMM-HMRF is marked by the black dotted line. MICO is marked by the green chain line.

The analyses of the seed threshold are shown in Fig.8. For Fig.8(a), the RAE of GSRG is lower than that of three comparison methods with the seed threshold from 0.02 to 0.788. The partially enlarged image of the ME curve is shown in Fig.8(c). The minimal ME of GSRG is 0.010 at the seed threshold of 0.7. When the seed threshold varies from 0.81 to 1, the ME of GSRG is higher than that of Otsu and increases exponentially. The IoU is shown in Fig.8(d). The IoU of GSRG is higher than the compared methods with the seed threshold between 0.62 and 0.825. The maximal IoU of GSRG is 0.567 at the seed threshold of 0.76. Hence, GSRG

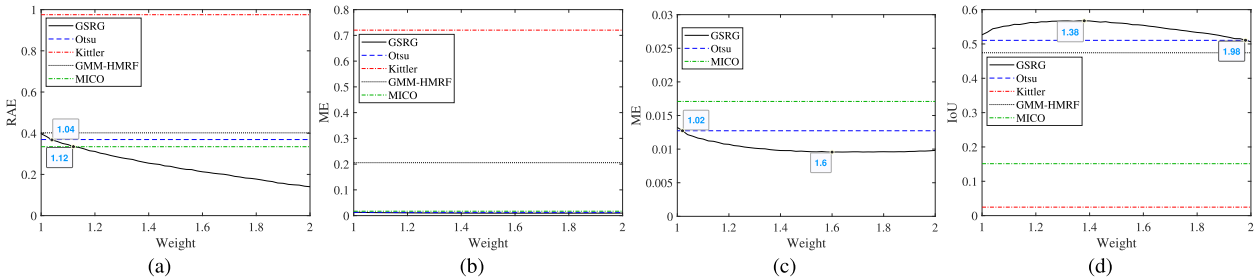

FIGURE 10. The analysis results of the weight. (a)The RAE. The intersection of GSRG and MICO is at (1.12,0.335). The intersection of GSRG and Otsu is at (1.04,0.369). (b)The ME. (c)The partially enlarged image of the ME curve. The intersection of GSRG and Otsu is at (1.02,0.013). The minimal ME of GSRG is at (1.6,0.010). (d)The IoU. The intersection of GSRG and Otsu is at (1.98,0.511). The maximal IoU of GSRG is at (1.38,0.567).

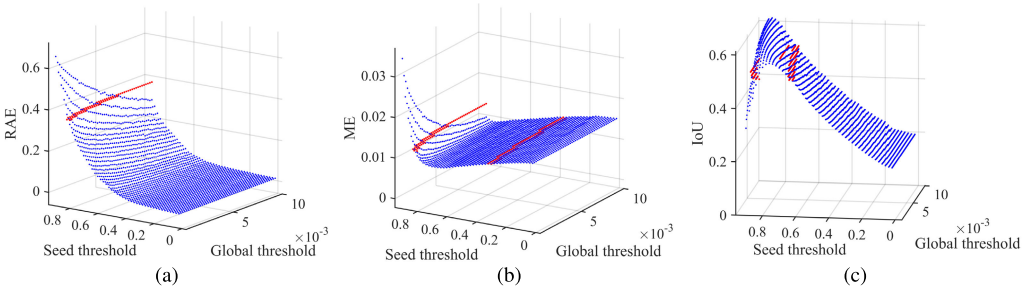

FIGURE 11. The joint analysis results of the seed threshold and the global threshold. The results of GSRG and Otsu are marked by the blue dots and the red dots respectively. (a)The RAE. (b)The ME. (c)The IoU.

has a good performance when the seed threshold is between 0.62 and 0.81.

The analyses of the global threshold are shown in Fig.9. For Fig.9(a), the RAE of GSRG is always lower than that of the comparison methods and decreasing with the global threshold from 0.0001 to 0.01. Fig.9(c) shows the partially enlarged image of the ME curve. The ME of GSRG is also consistently lower than that of the comparison methods. Differently, the ME of GSRG has a decreasing with the global threshold from 0.0001 to 0.0013 and an increasing with the global threshold from 0.0013 to 0.01. The minimal ME of GSRG is about 0.009 at the global threshold of 0.0013. For Fig.9(d), the IoU of GSRG is decreasing continuously and higher than that of Otsu with the global threshold from 0.0001 to 0.0062. Considering, GSRG has a good performance when the global threshold is around 0.0013.

The analyses of the weight are shown in Fig.10. For Fig.10(a), the RAE of GSRG is decreasing continuously and lower than that of the comparison methods with the weight from 1.12 to 2. For Fig.10(c), when the weight is between 1.6 and 1.8, the ME of GSRG fluctuates at a low level. The minimal ME of GSRG is 0.010 at the weight of 1.6. For Fig.10(d), the IoU of GSRG is higher than that of Otsu with the weight from 1 to 1.98. The maximal IoU of GSRG is 0.567 at the weight of 1.38. Hence, GSRG has a good performance when the weight is between 1.38 and 1.6.

Briefly, the proposed algorithm has a good performance when the seed threshold is around 0.7, the global threshold is around 0.0013, and the weight is between 1.38 and 1.6.

TABLE 3. The setting of the two-parameter joint analyses.

Analyzed parameters	μ	δ	α
μ & δ	[0.02,0.9]	[0.0002,0.01]	1.6
μ & α	[0.02,0.9]	0.0001	[1,2]
δ & α	0.7	[0.0002,0.01]	[1,2]

According to the influences of three parameters on the evaluation criteria, the influence of the seed threshold μ is stronger than that of the weight α and that of the global threshold δ.

C. THE TWO-PARAMETER ANALYSIS

The independent influences of each parameter have been analyzed. Then, two-parameter joint analyses are implemented to reflect the algorithm characteristics comprehensively. The growing coefficient K and the enhancement coefficient γ are still controlled with $K = 1$ and $\gamma = 2$. The other three parameters are analyzed. For two-parameter joint analyses, one parameter is fixed, and two parameters vary within the settings. The setting of the parameters is specified in Table 3. We only use Otsu as the compared method.

The joint analyses are illustrated in Fig.11, Fig.12, Fig.13. In these figures, GSRG surface consists of blue dots, and Otsu surface consists of the red dots. Because Otsu surface is flat, only the red dots near the intersection of the two methods are shown to avoid the two surfaces occlude each other.

The influence of the seed threshold and the global threshold on GSRG is displayed in Fig.11. As shown in Fig.11(a), the RAE of GSRG is lower than that of Otsu with the

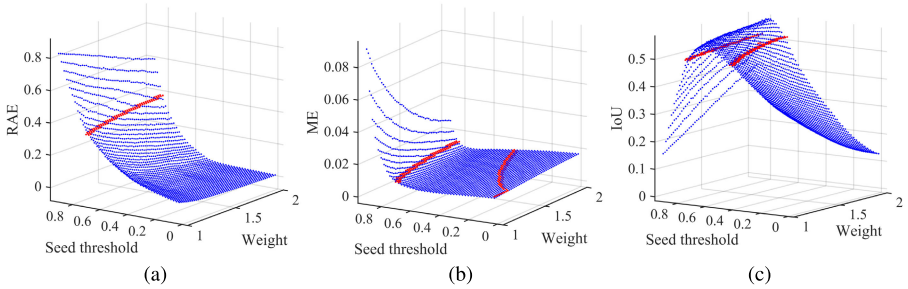

FIGURE 12. The joint analysis results of the seed threshold and the weight. The results of GSRG and Otsu are marked by the blue dots and the red dots respectively. (a)The RAE. (b)The ME. (c)The IoU.

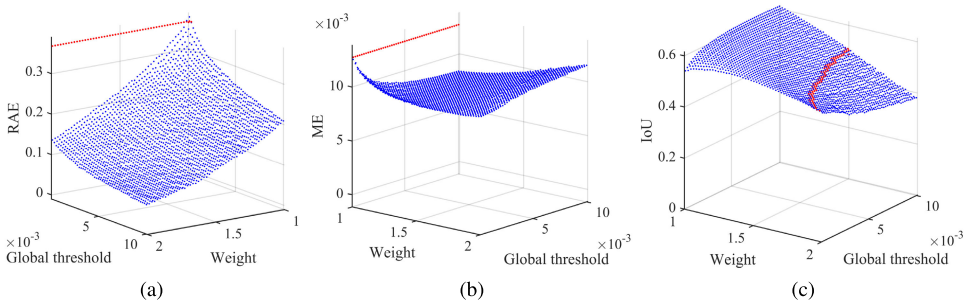

FIGURE 13. The joint analysis results of the global threshold and the weight. The results of GSRG and Otsu are marked by the blue dots and the red dots respectively. (a)The RAE. (b)The ME. (c)The IoU.

seed threshold from 0.02 to 0.8. For Fig.11(b), the ME of GSRG reaches the bottom with the seed threshold between 0.7 and 0.8. Simultaneously, the IoU of GSRG reaches the top, which is shown in Fig.11(c). Comprehensively, the influence of the seed threshold is much stronger than that of the global threshold. The global threshold has little effect with the seed threshold smaller than 0.4. The influence of the global threshold is increasing with the seed threshold from 0.4 to 0.9. Especially when the seed threshold is larger than 0.8, the performance of GSRG is still better than Otsu with the global threshold higher than 0.006. Hence, GSRG has good performance when the seed threshold is around 0.7, and the global threshold is higher than 0.006.

The influence of the seed threshold and the weight on GSRG is shown in Fig.12. For Fig.12(a), the RAE of GSRG is lower than that of Otsu with the seed threshold between 0.02 and 0.7. The trend of Fig.12(b) and Fig.12(c) is similar to the trend of Fig.11(b) and Fig.11(c). The ME of GSRG reaches the bottom with the seed threshold between 0.6 and 0.7, simultaneously, the IoU of GSRG reaches the top. Similar to the relation between the seed threshold and the global threshold, the influence of the seed threshold is larger than that of the weight. Differently, the influence of the weight is lower than that of the global threshold. When the seed threshold is larger than 0.8, the performance of GSRG is worse than that of Otsu no matter how the weight changes. Hence, GSRG has good performance when the seed threshold is around 0.6 and the weight is close to 1.

The influence of the global threshold and the weight is displayed in Fig.13. As shown in Fig.13(a) and (b), the RAE and the ME of GSRG are almost always smaller than those of Otsu. For Fig.13(c), when the weight is smaller than about 1.5, the IoU of GSRG is better than that of Otsu. For Fig.13, the influence of the weight is stronger than that of the global threshold with the seed threshold 0.7. Both the RAE and the IoU are inversely proportional to the weight and the global threshold. Hence, GSRG has good performance when the weight is around 1.5 and the global threshold is close to 0.01.

Consequently, compared with the results of three two-parameter joint analyses, the influence of the weight and the global threshold is lower than that of the seed threshold. The influence of the weight and the global threshold is increasing with the increasing of the seed threshold. GSRG has good performance when the seed threshold is between 0.6 and 0.7, the weight is around 1.5, and the global threshold is close to 0.01. The results of the two-parameter analysis are almost consistent with the results of the single parameter analysis.

V. EXPERIMENT

A. PROCESSING ON SIMPLE TARGET

1) SETTINGS

For the experiment of the simple target, the planar array system is implemented to obtain the echo of the scissors, the pistol, and the rifle. The carrier frequency is 30 GHz, and the bandwidth is 12.8 GHz. The size of the planar array is 0.8 m $\times$ 2 m, and the element number of the planar array is 160 $\times$ 400. Back projection is applied to achieve 3D SAR imaging, and the image size is 160$\times$400$\times$20.

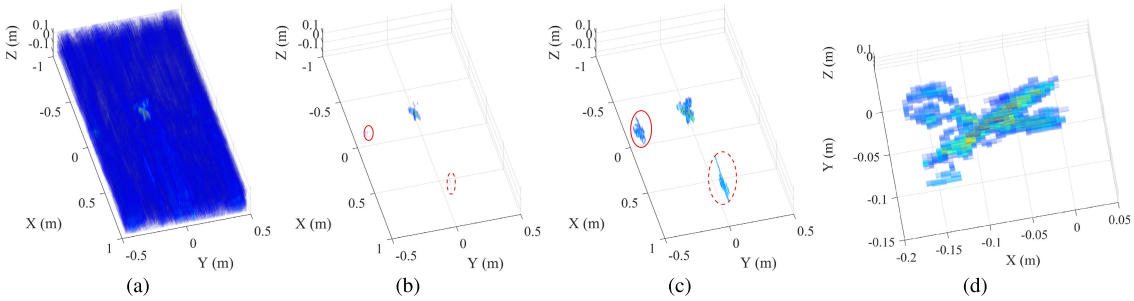

FIGURE 14. The process and the result of the scissors. The grating lobe is marked by the red solid circle. The interference is marked by the red dotted circle. (a)The original SAR image. (b)The seed matrix. (c)The result of GSRG. (d)The enlarged image.

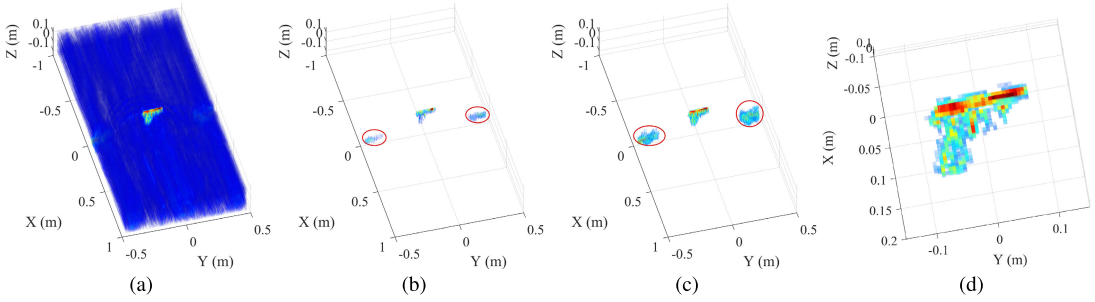

FIGURE 15. The process and the result of the pistol. The grating lobe is marked by the red solid circle. (a)The original SAR image. (b)The seed matrix. (c)The result of GSRG. (d)The enlarged image.

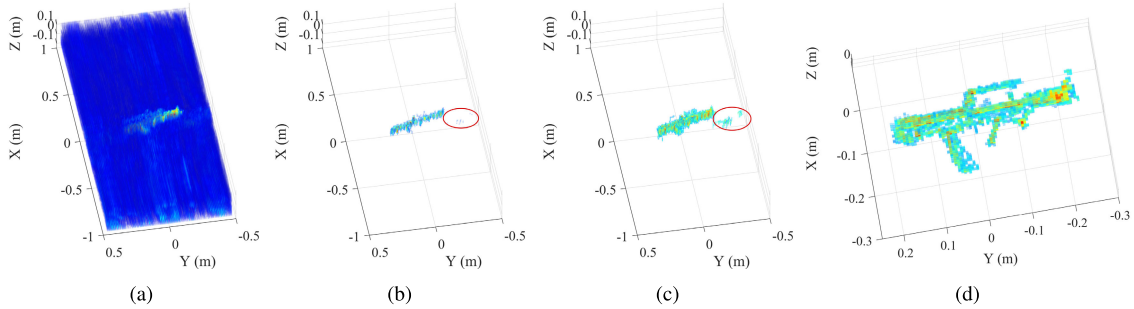

FIGURE 16. The process and the result of the rifle. The grating lobe is marked by the red solid circle. (a)The original SAR image. (b)The seed matrix. (c)The result of GSRG. (d)The enlarged image.

TABLE 4. The parameter setting of the proposed method.

Parameter	Scissors	Pistol	Rifle
Weight α	6.9	1	1.2
Seed threshold μ	0.7	0.7	0.68
Global threshold δ	0.0004	0.0001	0.0001

The parameters of the proposed method are set as follows: The growing coefficient K is 1. The enhancement coefficient γ is 2. The other parameters are specified in Table 4. Otsu, Kittler, GMM-HMRF, and MICO are applied as the compared methods. The RAE, the ME, and the IoU are applied as the evaluation criteria.

2) RESULTS

The background separation results of three targets are respectively illustrated in Fig.14, Fig.15, and Fig.16. The original 3D SAR image of three targets is shown in the sub-figure (a) of Fig.14, Fig.15, and Fig.16. Obviously, the backgrounds of the experiment images are much more complicated than the background of the simulation image. Space is not only full of noise but also has strong environmental interference distributed around the target.

The seed matrix is extracted by the weighted Otsu and shown in the sub-figure (b) of Fig.14, Fig.15, and Fig.16. For the pistol and the rifle displayed in Fig.15(b) and Fig.16(b) respectively, there is almost no interference contained in the seeds. The grating lobes marked by the red solid circle are on the side of the target. For the scissors displayed in Fig.14(b), there is some interference marked by the red dotted circle and a few grating lobes marked by the red solid circle. A little interference still exists in the seeds because the amplitude of the strong interference is close to that of the scissors' details. For the sub-figure (b) of Fig.14, Fig.15, and Fig.16, there

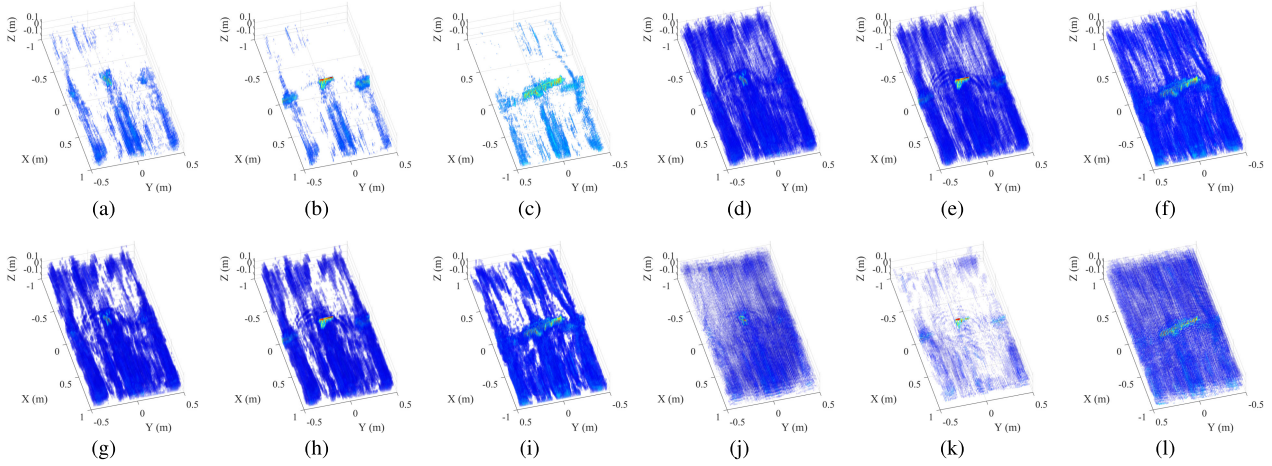

FIGURE 17. The background separation results processed by the comparison methods. (a)Scissors (Kittler). (b)Pistol (Kittler). (c)Rifle (Kittler). (d)Scissors(Otsu). (e)Pistol (Otsu). (f)Rifle (Otsu). (g)Scissors (GMM-HMRF). (h)Pistol (GMM-HMRF). (i)Rifle (GMM-HMRF). (j)Scissors (MICO). (k)Pistol (MICO). (l)Rifle (MICO).

are a few grating lobes in all three seed matrices due to the amplitude of the grating lobes is close to that of the target. Generally, the distance between the target and the grating lobes is far enough. Therefore, the grating lobes will not influence the background separation.

For the seed extraction, the weight is applied to ensure the seeds do not contain the background as much as possible. The amplitude of the scissors is lower than that of the pistol and the rifle. Therefore, the seed extraction of the scissors is more difficult than that of the pistol and the rifle. No matter how difficult it is to extract the seeds, the weight ensures the seeds contain little background. Thus, the seeds of the scissors only contain a little background.

The seeds only include the main target information. The details will be restored by region growing. The growing results are shown in the sub-figure(c) of Fig.14, Fig.15, and Fig.16. For the pistol and the rifle, the interference almost cannot be observed in the growing result. For the scissors, the growing result only contains a little interference. Compared with sub-figure(b) and sub-figure(c) of Fig.14, Fig.15, and Fig.16, if there are backgrounds in the seed matrix, the backgrounds also have a growing while the target growing. Therefore, it is important to eliminate the background when the seed matrix is extracted. The weighted Otsu has a good performance on the seed extraction, thereby, the background separation results of three targets only contain a few backgrounds. To show the details of the processed result, the enlarged images of three targets are shown in the sub-figure (d) of Fig.14, Fig.15, and Fig.16. Not only is the background separated, but the target details are preserved. Hence, GSRG achieves background separation effectively.

The background separation results of the comparison methods are shown in Fig.17. Otsu, GMM-HMRF, and MICO can hardly eliminate the background. Especially, MICO eliminates a lot of target information while eliminating the background. Kittler can eliminate part of the background, however, the results are still unsatisfactory. Thus, the results of the comparison methods are worse than the results of GSRG.

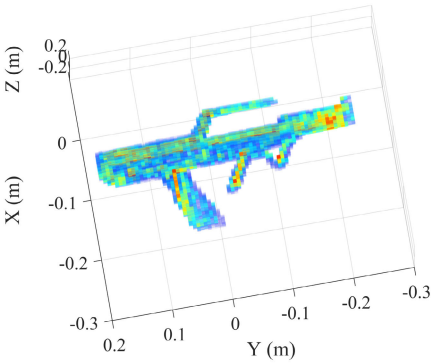

FIGURE 18. The ground truth of the rifle. It is used as the standard for the evaluation.

So far, intuitive evaluations have been finished. Then, the performance will be analyzed by three evaluation criteria, the RAE, the ME, and the IoU. The result of the rifle is selected and analyzed because it has a clear and complicated outline. The ground truth of the rifle is extracted from the original SAR image based on optical image, and shown in Fig.18. The performance of the five methods is calculated and reported in Table 5. Because of the poor stability of GMM-HMRF and MICO, 500 independent experiments are performed on MICO, and 200 independent experiments are performed on GMM-HMRF. The RAE, ME, and IoU of GMM-HMRF and MICO shown in Table 5 refer to the mean of the independent experiments. The RAE of GSRG is 75.59% lower than that of Otsu, 64.19% lower than that of Kittler, 75.96% lower than that of GMM-HMRF, and 75.55% lower than that of MICO. The ME of GSRG is 27.61% lower than that of Otsu, 2.09% lower than that of Kittler, 40.92%

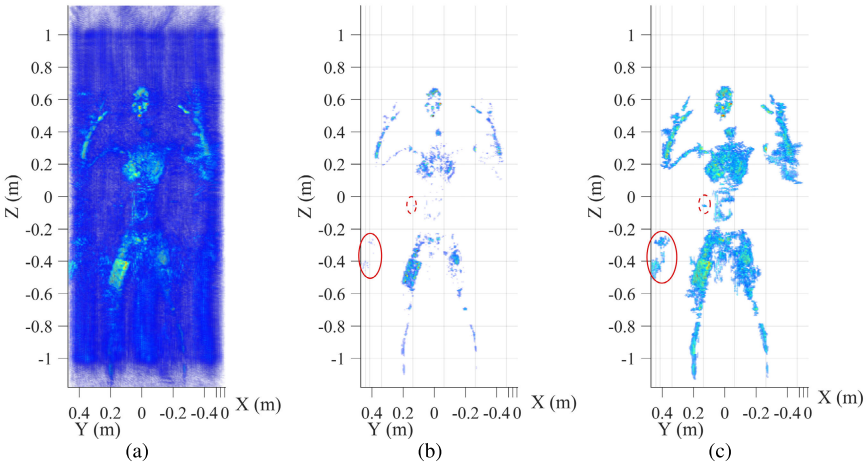

FIGURE 19. The process and the result of the human body. The grating lobe is marked by the red solid circle. The interference is marked by the red dotted circle. (a)Original SAR image. (b)Seed matrix. (c)Processed image by GSRG.

TABLE 5. The analysis results of the rifle.

Method	RAE	ME	IoU
GSRG	22.90%	0.27%	49.83%
Otsu	98.49%	27.88%	1.50%
Kittler	87.09%	2.36%	12.24%
GMM-HMRF	98.86%	41.19%	1.14%
MICO	98.45%	12.78%	1.21%

lower than that of GMM-HMRF, and 12.51% lower than that of MICO. The IoU of GSRG is 48.33% higher than that of Otsu, 37.59% higher than that of Kittler, 48.69% higher than that of GMM-HMRF, and 48.62% higher than that of MICO. Thus, the performance of GSRG is higher than that of the comparison methods. And the performance of GMM-HMRF is the worst.

Although the experiment images are more complicated than the simulation images, GSRG achieves the background separation of 3D SAR image effectively. Conversely, Otsu, GMM-HMRF, and MICO almost have no effect on background separation of 3D SAR image. Kittler has an effect on background separation, but the results of Kittler are still not satisfactory. After the intuitive and quantitative analyses, it is proved that the performance of GSRG is superior to that of the comparison methods.

B. PROCESSING ON COMPLICATED TARGET

1) SETTINGS

The complicated target is a human body with some foreign matters. The system parameters of the complicated target are the same as those of the simple target. The size of the SAR image is 160×400×20. The parameters of GSRG are set as follows: The seed threshold is 0.7. The global threshold is 0.0001. The weight is 1.3. The growing coefficient K is 1. The enhancement coefficient γ is 2. Otsu, Kittler, GMM-HMRF, and MICO are applied as the compared methods. The RAE, the ME, and the IoU are applied as the evaluation criteria.

2) RESULTS

The original SAR image is depicted in Fig.19(a). The seed matrix shown in Fig.19(b) contains a little interference marked by the red dotted circle and some grating lobes marked by the red solid circle. The result of GSRG is illustrated in Fig.19(c). GSRG not only achieves background separation effectively but also preserves the details of the human body and foreign matters. The results of four comparison methods are shown in Fig.20. For Fig.20(a), the result of Kittler is the best of the four comparison methods, however, it still contains lots of backgrounds. Otsu has some effect on the background separation, and the result is shown in Fig.20(b). The result of GMM-HMRF is similar to the result of Kittler, which is shown in Fig.20(c). MICO has little effect on the background separation, which is shown in Fig.20(d). The residual backgrounds in the results of the comparison methods are much more than that of GSRG. Thus, the performance of GSRG is much better than that of the four comparison methods.

In order to verify the effect of the global threshold on noise suppression, the proposed method without the global threshold is implemented on human body. And the result is shown in Fig.21. Compared with the result of GSRG shown in Fig.19(c), the result of GSRG without the global threshold contains additional noise marked by the red solid circle. Therefore, it is necessary to implement the global threshold to suppress the noise.

Finally, we will discuss the stability of these five methods. For Otsu and Kittler, the performance of Otsu and Kittler is different in the experiment and simulation. The result of Otsu in the simulation is acceptable, conversely, Otsu has little effect on background separation in the experiment. Similarly, Kittler has no effect on background separation

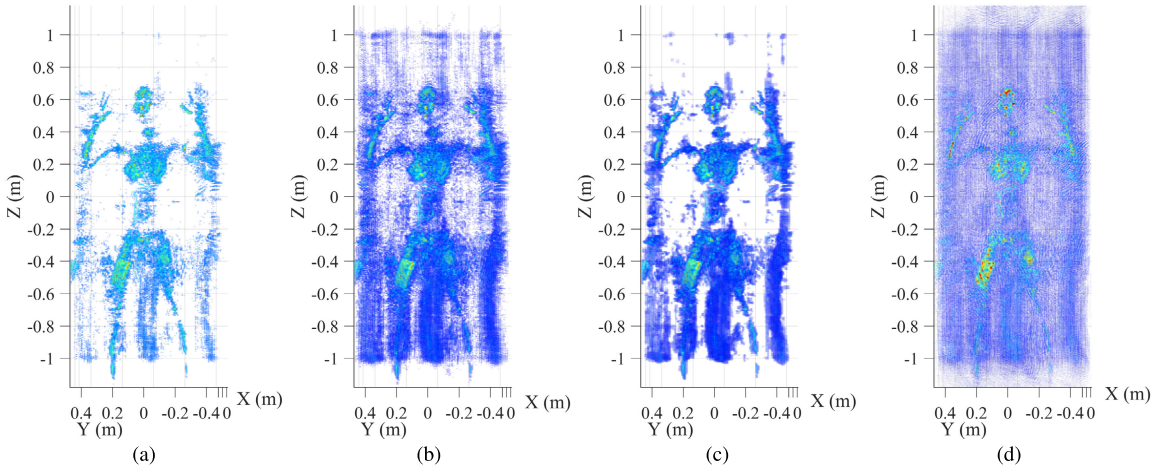

FIGURE 20. The results of the four compared methods. (a) The image processed by Kittler. (b) The image processed by Otsu. (c) The image processed by GMM-HMRF. (d) The image processed by MICO.

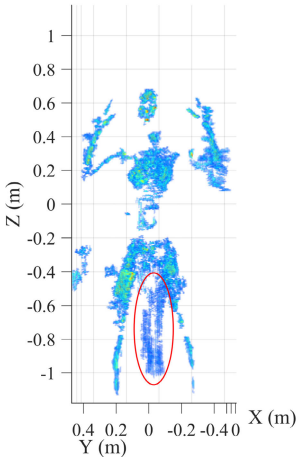

FIGURE 21. The process result of human body by GSRG without the global threshold.

in the simulation and has little effect on the experiment. Therefore, it is unstable for Otsu and Kittler to separate the background. For GMM-HMRF and MICO, the simulation image background can be separated by these two methods. However, these two methods cannot achieve the separation of the experiment image background which is much more complicated than the simulation image background. Therefore, these two methods are unsuitable for the separation of the complicated background. Moreover, the performance of GMM-HMRF and MICO is extremely unstable, which has shown in Fig.7.

Whether it is simulation or experiment, the proposed method is not affected by the changing of the target and the environment, and achieves the background separation stably and accurately. Consequently, both the performance and robustness of the proposed method are stronger than those of the comparison methods.

TABLE 6. The settings of the single parameter analyses.

Analyzed parameter	μ	δ	α
Seed threshold μ	[0.02,1]	0.0001	1
Global threshold δ	0.6	[0.0001,0.01]	1
Weight α	0.6	0.0001	[1,2]

C. THE SINGLE PARAMETER ANALYSIS

The single parameter analysis is implemented to analyze the influence of each parameter. The result of the rifle is selected and discussed. Same as the analyses in the simulation, the image evaluation criteria are still the RAE, the ME, and the IoU. The ground truth is shown in Fig.18. Otsu, Kittler, GMM-HMRF, and MICO are applied as the comparison methods. The growing coefficient K and the enhancement coefficient γ are controlled with $K = 1$ and $\gamma = 2$. The parameter settings are specified in Table 6. In each analysis, two parameters are fixed, one parameter varies within the setting. The analyses of GSRG are illustrated in Fig.22, 23, and 24. GSRG is marked by the black solid line. Otsu is marked by the blue dashed line. Kittler is marked by the red chain line. GMM-HMRF is marked by the black dotted line. MICO is marked by the green chain line.

The analyses of the seed threshold are displayed in Fig.22. For the ME shown in Fig.22(a), the RAE of GSRG is lower than that of the comparison methods with the seed threshold lower than 0.863. For the ME shown in Fig.22(b), the ME of GSRG is higher than that of Kittler with the seed threshold larger than 0.852 and begins to increase exponentially. The ME of GSRG is higher than that of MICO, OTSU, and GMM-HMRF when the seed threshold is higher than 0.919, 0.951, and 0.966 respectively. For Fig.22(c), the minimal ME of GSRG is 0.003 at the seed threshold of 0.56. For the IoU shown in Fig.22(d), the IoU of GSRG is superior

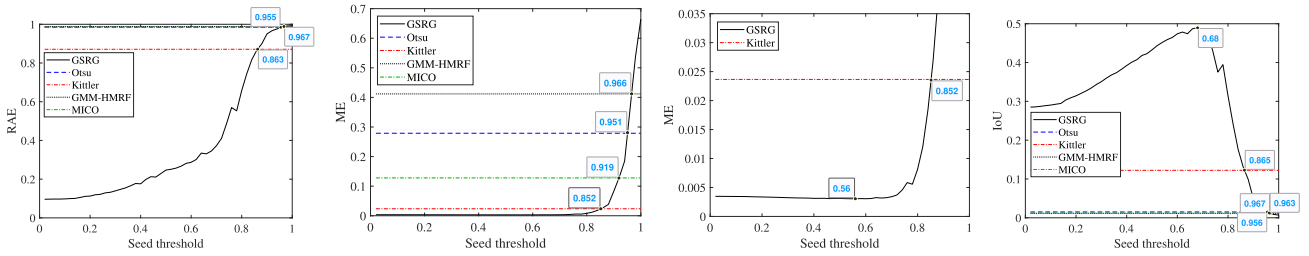

FIGURE 22. The analysis results of the seed threshold. (a)The RAE. The intersection of GSRG and Kittler is at (0.863,0.871). The intersection of GSRG and Otsu is at (0.955,0.985). The intersection of GSRG and MICO is at (0.955,0.985). The intersection of GSRG and GMM-HMRF is at (0.967,0.989). (b)The ME. The intersection of GSRG and Kittler is at (0.852,0.024). The intersection of GSRG and MICO is at (0.919,0.128). The intersection of GSRG and Otsu is at (0.951,0.279). The intersection of GSRG and GMM-HMRF is at (0.966,0.412). (c)The partially enlarged image of the ME curve. The intersection of GSRG and Kittler is at (0.852,0.024). The minimal ME of GSRG is at (0.56,0.003). (d)The IoU. The intersection of GSRG and GMM-HMRF is at (0.967,0.011). The intersection of GSRG and MICO is at (0.963,0.012). The intersection of GSRG and Otsu is at (0.956,0.015). The intersection of GSRG and Kittler is at (0.865,0.122). The maximal IoU of GSRG is at (0.68,0.489).

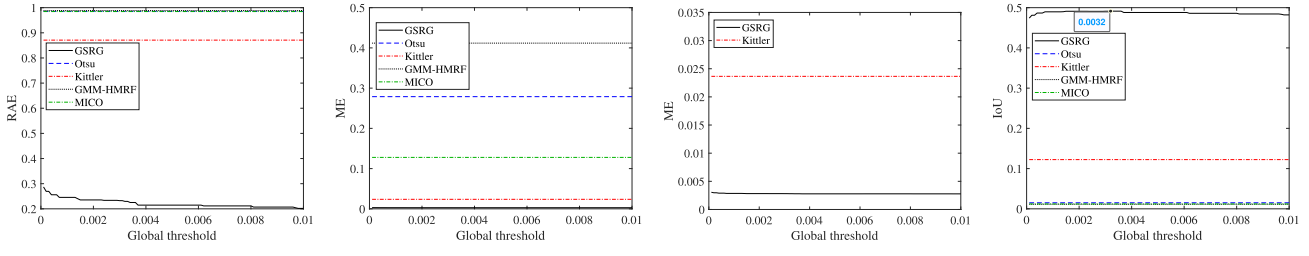

FIGURE 23. The analysis results of the global threshold. (a)The RAE. (b)The ME. (c)The partially enlarged image of the ME curve. (d)The IoU. The maximal IoU of GSRG is at (0.0032,0.491).

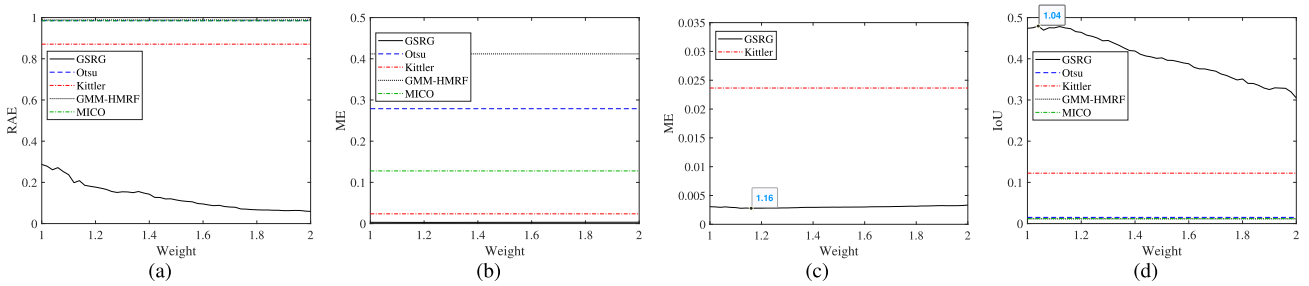

FIGURE 24. The analysis results of the weight. (a)The RAE. (b)The ME. (c)The partially enlarged image of the ME curve. The minimal ME of GSRG is at (1.16,0.003). (d)The IoU. The maximal IoU of GSRG is at (1.04,0.479).

to that of Kittler with the seed threshold lower than 0.865, and superior to that of OTSU, MICO, and GMM-HMRF with the seed threshold lower than about 0.96. The maximal IoU of GSRG is 0.489 at the seed threshold of 0.68. Hence, GSRG has high performance when the seed threshold is around 0.68.

The analyses of the global threshold are shown in Fig.23. The RAE and ME of GSRG are always lower than those of the compared methods. The IoU of GSRG is always higher than that of the compared methods. The maximal IoU of GSRG is 0.491 at the global threshold of 0.0032. Hence, GSRG has high performance when the global threshold is around 0.0032. The global threshold has little influence on GSRG with the seed threshold of 0.6 and the weight of 1.

The analyses of the weight are displayed in Fig.24. For the RAE shown in Fig.24(a), the RAE of GSRG has a continuous decreasing with the weight from 1 to 2. For the ME shown in Fig.24(c), the minimal ME of GSRG is 0.003 at the weight of 1.16. For the IoU shown in Fig.24(d), the maximal IoU of GSRG is 0.479 at the weight of 1.16. Hence, GSRG has high performance when the weight is around 1.16.

Consequently, GSRG has high performance when the seed threshold is around 0.68, the global threshold is around 0.0032, and the weight is around 1.16. The influence of the seed threshold is stronger than that of the global threshold and the weight. The results of the single parameter analysis in the experiment are similar to the results of the single parameter analysis in the simulation.

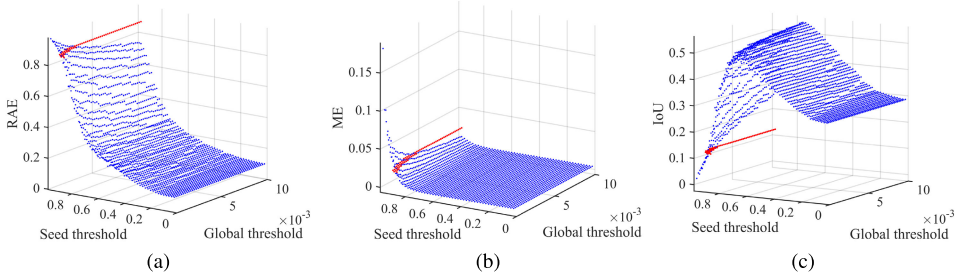

FIGURE 25. The joint analysis results of the seed threshold and the global threshold. The results of GSRG and Kittler are marked by the blue dots and the red dots respectively. (a) The RAE. (b) The ME. (c) The IoU.

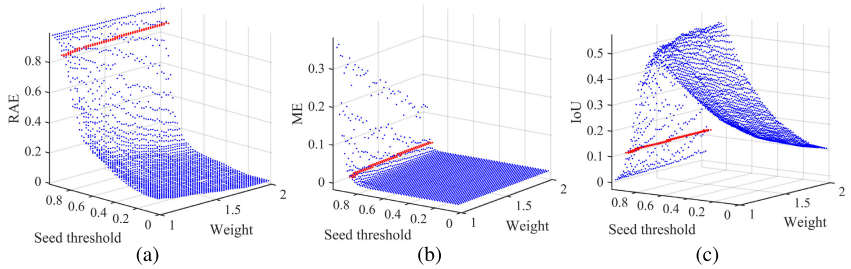

FIGURE 26. The joint analysis results of the seed threshold and the weight. The results of GSRG and Kittler are marked by the blue dots and the red dots respectively. (a) The RAE. (b) The ME. (c) The IoU.

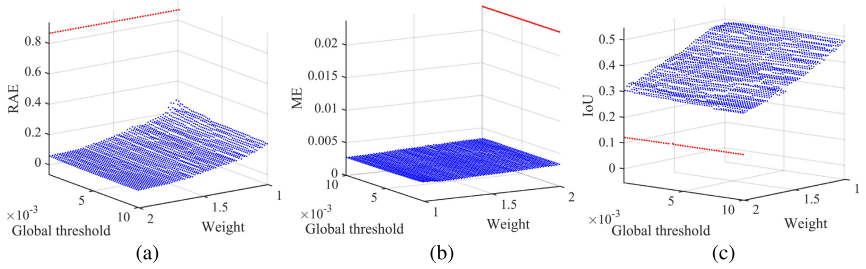

FIGURE 27. The joint analysis results of the global threshold and the weight with $\mu = 0.6$. The results of GSRG and Kittler are marked by the blue dots and the red dots respectively. (a) The RAE. (b) The ME. (c) The IoU.

D. THE TWO-PARAMETER ANALYSIS

The two-parameter joint analysis is implemented to reflect the algorithm characteristics comprehensively. Except for the parameters and the comparison method, the settings of the two-parameter joint analysis are the same as the settings of the single parameter analysis. The proposed method is compared with Kittler. The growing coefficient K and the enhancement coefficient γ are controlled with $K = 1$ and $\gamma = 2$. The settings of the other three parameters are specified in Table 7. For the two-parameter joint analysis, one parameter is fixed, two parameters vary within the settings. The analysis results are shown in Fig.25, Fig.26, and Fig.27.

The joint analyses of the seed threshold and the global threshold are displayed in Fig.25. For the RAE shown in Fig.25(a), the RAE of GSRG is increasing and higher than that of Kittler with the seed threshold higher than around 0.9. For the ME shown in Fig.25(b), the ME of GSRG has no significant change with the seed threshold from 0.02 to 0.8 and increases sharply with the seed threshold from 0.8 to 0.96. For the IoU shown in Fig.25(c), when the seed threshold is around 0.72, the IoU of GSRG reaches a maximum. Hence, GSRG has high performance when the seed threshold is around 0.72 and the global threshold is close to 0.01.

TABLE 7. The settings of the two-parameter joint analyses.

Analyzed parameters	μ	δ	α
μ & δ	[0.02,0.96]	[0.0002,0.01]	1
μ & α	[0.02,0.96]	0.0001	[1,2]
δ & α	0.6	[0.0002,0.01]	[1,2]

The joint analyses of the seed threshold and the weight are displayed in Fig.26. For the RAE shown in Fig.26(a),

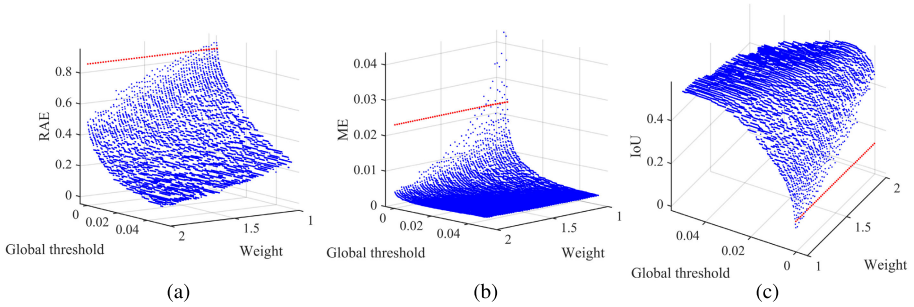

FIGURE 28. The joint analysis results of the global threshold and the weight with $\mu = 0.9$. The results of GSRG and Kittler are marked by the blue dots and the red dots respectively. (a) The RAE. (b) The ME. (c) The IoU.

TABLE 8. The computational cost of the simulation and the experiment.

Measured value	Aircraft model	Scissors	Pistol	Rifle	Human body
Image size	250×250×151	160×400×20	160×400×20	160×400×20	160×400×20
The number of the initial seeds	33380	484	929	1511	7774
The number of the increased pixels	109116	2201	2753	3187	31902
Time consuming (GSRG)	67.75s	4.26s	2.70s	2.49s	23.24s
Time consuming (Otsu)	0.04s	0.01s	0.006s	0.006s	0.005s
Time consuming (Kittler)	0.35s	0.04s	0.05s	0.04s	0.05s
Time consuming (MICO)	285.42s	146.33s	146.11s	146.20s	152.10s
Time consuming (GMM-HMRF)	71.64s	86.15s	77.47s	90.72s	73.25s

the RAE of GSRG is increasing and higher than that of Kittler with the seed threshold higher than around 0.8. For the ME shown in Fig.26(b), neither the seed threshold nor the weight has an effect on the ME of GSRG with the seed threshold from 0.02 to 0.8 and the weight from 1 to 2. However, the ME of GSRG increases exponentially with the seed threshold from 0.8 to 0.96. For the IoU shown in Fig.26(c), the maximal IoU of GSRG is at around the seed threshold 0.8. Hence, GSRG has high performance when the seed threshold is around 0.8, and the weight is close to 2.

The joint analyses of the global threshold and the weight are displayed in Fig.27. The performance of GSRG is always better than that of Kittler with the seed threshold of 0.6. For the ME shown in Fig.27(b), both two parameters have little effect on the ME of GSRG. For the RAE and the IoU shown in Fig.27(a) and (c) respectively, both the RAE and the IoU are increasing with the decreasing of the weight, and the RAE is increasing with the decreasing of the global threshold. Compared with the global threshold, the weight has more influence on the RAE and the IoU. Hence, GSRG has high performance when the weight is around 1.5 and the global threshold is close to 0.01.

Same as the results of the two-parameter joint analysis in the simulation, the influence of the seed threshold is higher than the influence of the global threshold and the weight. The global threshold and the weight have different impact capabilities with different seed threshold. To discuss the influence of the global threshold and the weight with a high seed threshold, another analysis is implemented with the seed threshold of 0.9, the global threshold from 0.0002 to 0.05, and the weight from 1 to 2. The results are shown in Fig.28.

For the RAE shown in Fig.28(a), with the decreasing of the global threshold and the weight, the RAE of GSRG has a huge linearly increasing. For the ME shown in Fig.28(b), the ME of GSRG has an exponentially increasing with the global threshold from 0.01 to 0.0002 and the weight from 1.8 to 1. For the IoU shown in Fig.28(b), when the global threshold is between 0.02 to 0.05, the IoU of GSRG is increasing with the decreasing of the weight. When the global threshold is between 0.0002 to 0.02, the IoU of GSRG is decreasing with the decreasing of the weight. Therefore, the influence of the global threshold and the weight is related to the seed threshold. When the seed threshold is close to 1, the global threshold and the weight have a huge influence on the performance of GSRG, and ensure that the performance of GSRG does not decrease significantly.

In summary, the simulation and the experiment have the same analysis result. The seed threshold is more influential than the global threshold and weight. The effect of the global threshold and weight continuously increases with the increasing of the seed threshold. In the case where the weight ensures that the seeds contain little background, GSRG has good performance when the seed is around 0.7 and the global threshold is close to 0.01.

E. THE COMPUTATIONAL COST ANALYSIS

The proposed method and the comparison methods are tested on a computer with AMD Ryzen 1950X @3.4GHz, 64G memory, and GeForce GTX1080. The computational costs are recorded and shown in Table 8. This table also encompasses the image size, the number of initial seeds, and

the number of increased pixels. Otsu and Kittler achieve image segmentation by the histogram threshold. This kind of method has a simple calculation process. Therefore, Otsu and Kittler have huge advantages in computational cost. Although the computational cost of the proposed method is higher than that of Otsu and Kittler, it is significantly lower than that of MICO and GMM-HMRF.

Then, we will analyze the factors that affect the computational cost of the proposed method. The image size of the aircraft model is about 7.4 times that of the other four images, correspondingly, the time consuming of the aircraft model is the highest. Therefore, the computational cost is related to the image size. The scissors, the pistol, the rifle, and the human body have the same image size, however, the computational cost of the human body is much higher than that of the other three images. As shown in Table 8, the increased pixel number of the human body is much more than that of the other three images. Therefore, the computational cost is related to the number of increased pixels. For the scissors, the pistol, and the rifle, the ratio of the increased pixel number to the initial seed number is 4.548, 2.963, and 2.109 respectively. Correspondingly, the computational cost of the scissors, the pistol, and the rifle is 4.26s, 2.70s, and 2.49s respectively. Therefore, the computational cost is not only related to the image size and the number of increased pixels but also influenced by the ratio of the increased pixel number to the initial seed number.

VI. CONCLUSION

This paper presents a background separation method to achieve the eliminating of the noise and the interference in 3D SAR image. The image enhancement function, constructed with the real and the imagery information of SAR image, is implemented to suppress the noise and the weak interference. Due to the complexity of the target shape and the large dynamic range of the SAR image, the initial seeds are extracted by the weighted Otsu, and the weight ensures the initial seeds contain little background as much as possible. To suppress the increasing of the background during the region growing, the growing rate function is constructed by the amplitude of the initial seed and the current growing position. The seed threshold is used to restrict the growing of each seed independently. However, it is possible that the seed whose amplitude is close to the noise amplitude has an almost unrestricted growing, which will result in the process result with the noise-filled and low-quality. Therefore, the global threshold is applied to control the region growing via restricting the backward difference of the mask standard deviation.

The simulation and experiments not only verify the effectiveness of the proposed algorithm but also prove that the results of the proposed algorithm are far superior to the results of the four comparison methods. Besides, the performance of the proposed algorithm is analyzed by three image evaluation criteria with four comparison methods. For the analyzing results, the performance of the proposed algorithm is 0.31% to 76.27% better than that of the comparison methods.

The influence of three important parameters is investigated by fixing one or two parameters and changing the other parameters. The analysis results present that the seed threshold determines the background separation result directly. The effect of the weight and the global threshold on the performance of GSRG is proportional to the seed threshold.

Compared with other image segmentation methods, the proposed method also needs to adjust the parameters to obtain the best performance, which may be a limitation. We will find solutions to achieve the automatic 3D SAR image background separation in our future work. In other fields, there are already some automatic image segmentation methods, which can be the reference for the realization of automatic 3D SAR image background separation. We will present an automatic 3D SAR image background separation method in the next paper.

REFERENCES

[1] J. Klare, M. Weiss, O. Peters, A. Brenner, and J. Ender, "ARTINO: A new high resolution 3D imaging radar system on an autonomous airborne platform," in *Proc. IEEE Int. Symp. Geosci. Remote Sens.*, Jul./Aug. 2006, pp. 3842–3845.

[2] J. Klare, "Digital beamforming for a 3D MIMO SAR—Improvements through frequency and waveform diversity," in *Proc. IEEE Int. Geosci. Remote Sensing Symp. (IGARSS)*, vol. 5, Jul. 2008, pp. V-17–V-20.

[3] W. Xin, Z. Lu, G. Weihua, and F. Pcng, "Active millimeter-wave near-field cylindrical scanning three-dimensional imaging system," in *Proc. Int. Conf. Microw. Millim. Wave Technol. (ICMMT)*, May 2018, pp. 1–3.

[4] A. Pedross-Engel, D. Arnitz, J. N. Gollub, O. Yurduseven, K. P. Trofatter, M. F. Imani, T. Sleasman, M. Boyarsky, X. Fu, D. L. Marks, D. R. Smith, and M. S. Reynolds, "Orthogonal coded active illumination for millimeter wave, massive-MIMO computational imaging with metasurface antennas," *IEEE Trans. Comput. Imag.*, vol. 4, no. 2, pp. 184–193, Jun. 2018.

[5] Z. Guangfeng and Y. Changchang, "A passive MMW radiometric image feature extraction for security inspection," in *Proc. 13th IEEE Int. Conf. Electron. Meas. Instrum. (ICEMI)*, Oct. 2017, pp. 526–530.

[6] S. Gui, J. Li, and Y. Pi, "Security imaging for multi-target screening based on adaptive scene segmentation with terahertz radar," *IEEE Sensors J.*, vol. 19, no. 7, pp. 2675–2684, Apr. 2019.

[7] J. K. Gao, Z. M. Cui, B. B. Cheng, Y. L. Qin, X. J. Deng, B. Deng, X. Li, and H. Q. Wang, "Fast three-dimensional image reconstruction of a standoff screening system in the terahertz regime," *IEEE Trans. THz Sci. Technol.*, vol. 8, no. 1, pp. 38–51, Jan. 2018.

[8] D. A. Robertson, D. G. Macfarlane, R. I. Hunter, S. L. Cassidy, N. Llombart, E. Gandini, T. Bryllert, M. Ferndahl, H. Lindström, H. Vasama, J. Huopana, T. Selkälä, A.-J. Vuotikka, and J. Tenhunen, "A high frame rate, 340 GHz 3D imaging radar for security," in *Proc. IEEE Radar Conf. (RadarConf)*, Apr. 2018, pp. 55–60.

[9] Y. Zhao, X. Deng, B. Cheng, and J. Liu, "0.14 THz imaging system for security and surveillance," in *Proc. 42nd Int. Conf. Infr., Millim., THz. Waves (IRMMW-THz)*, Aug./Sep. 2017, pp. 1–2.

[10] K. Liao, X. Zhang, and J. Shi, "Plane-wave synthesis and RCS extraction via 3-D linear array SAR," *IEEE Antennas Wireless Propag. Lett.*, vol. 14, pp. 994–997, 2015.

[11] L. Xu, J. Li, Y. Shu, and J. Peng, "SAR image denoising via clustering-based principal component analysis," *IEEE Trans. Geosci. Remote Sens.*, vol. 52, no. 11, pp. 6858–6869, Nov. 2014.

[12] W. Zhao, C.-A. Deledalle, L. Denis, H. Maître, J.-M. Nicolas, and F. Tupin, "Ratio-based multitemporal SAR images denoising: RABASAR," *IEEE Trans. Geosci. Remote Sens.*, vol. 57, no. 6, pp. 3552–3565, Jun. 2019.

[13] C.-A. Deledalle, L. Denis, F. Tupin, A. Reigber, and M. Jäger, "NL-SAR: A unified nonlocal framework for resolution-preserving (Pol)(In)SAR denoising," *IEEE Trans. Geosci. Remote Sens.*, vol. 53, no. 4, pp. 2021–2038, Apr. 2015.

[14] F. Sica, D. Cozzolino, X. X. Zhu, L. Verdoliva, and G. Poggi, "InSAR-BM3D: A nonlocal filter for SAR interferometric phase restoration," *IEEE Trans. Geosci. Remote Sens.*, vol. 56, no. 6, pp. 3456–3467, Jun. 2018.

[15] P. Wang, H. Zhang, and V. M. Patel, "SAR image despeckling using a convolutional neural network," *IEEE Signal Process. Lett.*, vol. 24, no. 12, pp. 1763–1767, Dec. 2017.
[16] N. Otsu, "A threshold selection method from gray-level histograms," *IEEE Trans. Syst., Man, Cybern.*, vol. SMC-9, no. 1, pp. 62–66, Jan. 1979.
[17] R. Adams and L. Bischof, "Seeded region growing," *IEEE Trans. Pattern Anal. Mach. Intell.*, vol. 16, no. 6, pp. 641–647, Jun. 1994.
[18] V. R. P. Borges, M. C. F. de Oliveira, T. G. Silva, A. A. H. Vieira, and B. Hamann, "Region growing for segmenting green microalgae images," *IEEE/ACM Trans. Comput. Biol. Bioinf.*, vol. 15, no. 1, pp. 257–270, Jan./Feb. 2018.
[19] T. Lan, S. Gao, J. Chi, and Y. Zhou, "Object contour extraction based salience detection and automatic region growing," in *Proc. Int. Conf. Virtual Reality Visualizat. (ICVRV)*, Sep. 2016, pp. 57–64.
[20] M. Ma, J. Liang, M. Guo, Y. Fan, and Y. Yin, "SAR image segmentation based on artificial bee colony algorithm," *Appl. Soft Comput.*, vol. 11, pp. 5205–5214, Dec. 2011.
[21] P. Yu, A. K. Qin, and D. A. Clausi, "Unsupervised polarimetric SAR image segmentation and classification using region growing with edge penalty," *IEEE Trans. Geosci. Remote Sens.*, vol. 50, no. 4, pp. 1302–1317, Apr. 2012.
[22] Z. Jin, T. Tillo, W. Zou, Y. Zhao, and X. Li, "Robust plane detection using depth information from a consumer depth camera," *IEEE Trans. Circuits Syst. Video Technol.*, vol. 29, no. 2, pp. 447–460, Feb. 2019.
[23] P. Lu, K. Du, W. Yu, R. Wang, Y. Deng, and T. Balz, "A new region growing-based method for road network extraction and its application on different resolution SAR images," *IEEE J. Sel. Topics Appl. Earth Observ. Remote Sens.*, vol. 7, no. 12, pp. 4772–4783, Dec. 2014.
[24] S. Leigh, Z. Wang, and D. A. Clausi, "Automated ice–water classification using dual polarization SAR satellite imagery," *IEEE Trans. Geosci. Remote Sens.*, vol. 52, no. 9, pp. 5529–5539, Sep. 2014.
[25] E. Kozegar, M. Soryani, H. Behnam, M. Salamati, and T. Tan, "Mass segmentation in automated 3-D breast ultrasound using adaptive region growing and supervised edge-based deformable model," *IEEE Trans. Med. Imag.*, vol. 37, no. 4, pp. 918–928, Apr. s2018.
[26] X. Hua, J. Qian, H. Zhao, L. Liu, L. Liu, and Y. Wu, "Automatic intestinal canal segmentation based region growing with multi-scale entropy," in *Proc. IEEE 3rd Int. Conf. Image, Vis. Comput. (ICIVC)*, Jun. 2018, pp. 273–277.
[27] F. Bozkurt, C. Köse, and A. San, "Comparison of seeded region growing and random walk methods for vessel and bone segmentation in CTA images," in *Proc. 10th Int. Conf. Electr. Electron. Eng. (ELECO)*, Nov./Dec. 2017, pp. 561–567.
[28] C. Revol-Müller, F. Peyrin, Y. Carrillon, and C. Odet, "Automated 3D region growing algorithm based on an assessment function," *Pattern Recognit. Lett.*, vol. 23, nos. 1–3, pp. 137–150, 2002.
[29] J. Dehmeshki, H. Amin, M. Valdivieso, and X. Ye, "Segmentation of pulmonary nodules in thoracic CT scans: A region growing approach," *IEEE Trans. Med. Imag.*, vol. 27, no. 4, pp. 467–480, Apr. 2008.
[30] G. Fu, H. Lu, J. K. Tan, H. Kim, X. Zhu, and J. Lu, "Segmentation of spinal canal region in CT images using 3D region growing technique," in *Proc. Int. Conf. Inf. Commun. Technol. Robot. (ICT-ROBOT)*, Sep. 2018, pp. 1–4.
[31] O. Ronneberger, P. Fischer, and T. Brox, "U-net: Convolutional networks for biomedical image segmentation," in *Proc. Int. Conf. Med. Image Comput. Comput.-Assist. Intervent.* Cham, Switzerland: Springer, 2015, pp. 234–241.
[32] K. He, G. Gkioxari, P. Dollár, and R. Girshick, "Mask R-CNN," in *Proc. IEEE Int. Conf. Comput. Vis.*, Oct. 2017, pp. 2961–2969.
[33] Y. Zhou, J. Shi, X. Yang, C. Wang, D. Kumar, S. Wei, and X. Zhang, "Deep multi-scale recurrent network for synthetic aperture radar images despeckling," *Remote Sens.*, vol. 11, no. 21, p. 2462, 2019.
[34] R. D. Stewart, I. Fermin, and M. Opper, "Region growing with pulse-coupled neural networks: An alternative to seeded region growing," *IEEE Trans. Neural Netw.*, vol. 13, no. 6, pp. 1557–1562, Nov. 2002.
[35] Z. Huang, X. Wang, J. Wang, W. Liu, and J. Wang, "Weakly-supervised semantic segmentation network with deep seeded region growing," in *Proc. IEEE Conf. Comput. Vis. Pattern Recognit.*, Jun. 2018, pp. 7014–7023.
[36] F. Marie, L. Corbat, Y. Chaussy, T. Delavelle, J. Henriet, and J.-C. Lapayre, "Segmentation of deformed kidneys and nephroblastoma using case-based reasoning and convolutional neural network," *Expert Syst. Appl.*, vol. 217, pp. 282–294, Aug. 2019.
[37] X. Jiang, Y. Guo, H. Chen, Y. Zhang, and Y. Lu, "An adaptive region growing based on neutrosophic set in ultrasound domain for image segmentation," *IEEE Access*, vol. 7, pp. 60584–60593, 2019.
[38] W. Pu, J. Wu, X. Wang, Y. Huang, Y. Zha, and J. Yang, "Joint sparsity-based imaging and motion error estimation for BFSAR," *IEEE Trans. Geosci. Remote Sens.*, vol. 57, no. 3, pp. 1393–1408, Mar. 2019.
[39] W. Pu, Y. Huang, J. Wu, H. Yang, and J. Yang, "Fast compressive sensing-based SAR imaging integrated with motion compensation," *IEEE Access*, vol. 7, pp. 53284–53295, 2019.
[40] Y. Akyildiz and R. L. Moses, "Scattering center model for SAR imagery," *Proc. SPIE*, vol. 3869, pp. 76–85, Dec. 1999.
[41] W. A. Yasnoff, J. K. Mui, and J. W. Bacus, "Error measures for scene segmentation," *Pattern Recognit.*, vol. 9, no. 4, pp. 217–231, 1977.
[42] M. Sezgin and B. Sankur, "Survey over image thresholding techniques and quantitative performance evaluation," *J. Electron. Imag.*, vol. 13, no. 1, pp. 146–166, 2004.
[43] J. Kittler and J. Illingworth, "Minimum error thresholding," *Pattern Recognit.*, vol. 19, no. 1, pp. 41–47, 1986.
[44] Q. Wang, "GMM-based hidden Markov random field for color image and 3D volume segmentation," 2012, *arXiv:1212.4527*. [Online]. Available: https://arxiv.org/abs/1212.4527
[45] C. Li, J. C. Gore, and C. Davatzikos, "Multiplicative intrinsic component optimization (MICO) for MRI bias field estimation and tissue segmentation," *Magn. Reson. Imag.*, vol. 32, no. 7, pp. 913–923, Sep. 2014.

LIANG LI received the B.S. degree from the School of Computer and Communication Engineering, Northeastern University at Qinhuangdao, Qinhuangdao, China, in 2016. He is currently pursuing the Ph.D. degree in signal and information processing with the University of Electronic Science and Technology of China (UESTC).

His research interests include radar signal processing, SAR systems, and RCS measurements.

XIAOLING ZHANG received the B.S., M.Sc., and Ph.D. degrees in electronic engineering from the University of Electronic Science and Technology of China (UESTC), Chengdu, China, in 1985, 1988, and 2000, respectively.

In 2000, she joined UESTC, where she is currently a Professor. Her research interests include radar signal processing and classification/recognition.

LING PU received the B.S. degree in electronic engineering from the University of Electronic Science and Technology of China, Chengdu, China, in 2014, where he is currently pursuing the Ph.D. degree in signal and information processing.

His research interests include radar signal processing, SAR systems, and RCS measurements.

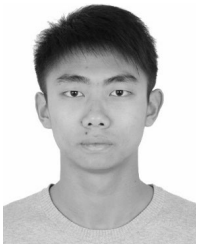

LIMING PU received the B.S. degree from the Nanjing University of Science and Technology, in 2016. He is currently pursuing the Ph.D. degree in signal and information processing with the University of Electronic Science and Technology of China, Chengdu, China.

His research interests include SAR imaging processing and interferometric synthetic aperture radar (InSAR) processing.

BOKUN TIAN received the B.S. degree in electronic engineering from the University of Electronic Science and Technology of China, Chengdu, China, in 2015, where he is currently pursuing the Ph.D. degree in signal and information processing.

His research interests include radar signal processing, SAR systems, and compressed sensing.

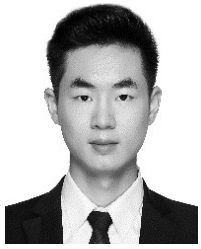

LIMING ZHOU received the B.Sc. degree in optoelectronic engineering from the University of Electronic Science and Technology of China (UESTC), Chengdu, China, in 2015, where he is currently pursuing the Ph.D. degree in signal and information processing.

His research interests include radar signal processing and MIMO SAR systems.

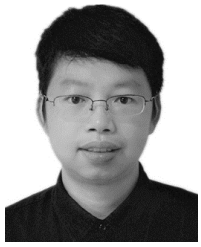

SHUNJUN WEI received the B.S., M.Sc., and Ph.D. degrees in electronic engineering from the University of Electronic Science and Technology of China (UESTC), Chengdu, China, in 2006, 2009, and 2013, respectively.

In 2014, he joined UESTC, where he is currently an Associate Professor. His research interests include radar signal processing and SAR systems.